A STUDY OF LITHOGRAPHY-BASED ADDITIVE MANUFACTURING OF CERIA CERAMICS

BY

RYAN FORDHAM

A THESIS
SUBMITTED TO THE FACULTY OF

ALFRED UNIVERSITY

IN PARTIAL FULFILLMENT OF THE REQUIREMENTS
FOR THE DEGREE OF

MASTER OF SCIENCE

IN

MATERIALS SCIENCE AND ENGINEERING

ALFRED, NEW YORK

AUGUST, 2021

A STUDY OF LITHOGRAPHY-BASED ADDITIVE MANUFACTURING OF CERIA CERAMICS

BY

Ryan Fordham

B.S. Alfred University (2019)

SIGNATURE OF AUTHOR_____

APPROVED BY_____

Dr. S. K. Sundaram, ADVISOR

_____

Dr. Holly Shulman, ADVISORY COMMITTEE

_____

Dr. Junjun Ding, ADVISORY COMMITTEE

_____

Dr. Seong-Jin Lee, CHAIR, ORAL THESIS DEFENSE

ACCEPTED BY_____

GABRIELLE G. GAUSTAD, DEAN
KAZUO INAMORI SCHOOL OF ENGINEERING

ACKNOWLEDGMENTS

I would first like to thank my graduate advisor, Dr. S. K. Sundaram, for his endless support and guidence through my graduate studies. He was always able and willing to help and answer any questions I had. I also would like to thank my committee members Dr. Holly Shulman and Dr. Junjun Ding for their help throughout my research and classwork. Shawn Allan and his team at Lithoz America LLC also provided great feedback and help throughout my research, in addition to physically helping with slurry development and testing. Also, Dean Gaustad and the whole of the School of Engineering administrative staff who gave me the support needed to complete my degrees. I would also like to acknowledge Dr. Darren Stohr and Jim Thiebaud for their assistance with the engineering school equipment and my undergraduate advisor Dr. Seong-Jin Lee for his support not only through my bachelors degree but also accepting me as his graduate teaching assistant. In addition, my fellow lab mates and graduate students; Nick, Tim, Kade, Dan, and John for giving me feedback and pushing me in the right direction when I needed it. Finally I'd like to thank my family John, Cyndi and Courtney for the encouragement and support I needed to always keep chugging along.

TABLE OF CONTENTS

Page

Acknowledgments ..... *iii*

Table of Contents ..... *iv*

List of Tables ..... *vi*

List of Figures ..... *vii*

Abstract ..... *xi*

I. INTRODUCTION 1

II. LITERATURE REVIEW 2

A. MATERIAL BACKGROUND 2

B. ADDITIVE MANUFACTURING OF CERAMICS 3

C. LITHOZ LCM PROCESS 5

D. CERIA SINTERING 7

III. EXPERIMENTAL PROCEDURE 9

A. PARAMETRIC STUDY 9

B. POWDER CHARACTERIZATION 10

C. SLURRY DEVELOPMENT 11

D. PRINTING PROCEDURE 11

E. BULK CHARACTERIZATION 15

IV. RESULTS AND DISCUSSION 17

A. POWDER CHARACTERIZATION 17

1. Powder Density 17

2. X-ray Diffraction (XRD) 17

3. Particle Size 18

B. SLURRY DEVELOPMENT 19

C. PRINTED SAMPLES 22

1. Bulk Density 22

2. Microstructure Characterization 28

3. XPS Analysis 43

4. Printing anomolies 46

V. SUMMARY AND CONCLUSIONS 49

VI. FUTURE WORK 51

VII. REFERENCES 52

IX. APPENDIX 55

LIST OF TABLES

Page

Table 1. Reference XPS BE Peaks for Ce $3d_{5/2}$ and Ce $3d_{3/2}$[18] 3

Table 2. AM Processes[21] 4

Table 3. (a) CeO_2 Preconditioning Schedule, (b) CeO_2 Debinding Schedule, and (c) CeO_2 Sintering Schedule 14

Table 4. Density Measurements of 0.5, 1, 2, and 10 µm Advertised CeO_2 Powders 17

Table 5. Powder Particle Size Measurements of 0.5, 1, 2, and 10 µm Advertised Powders 19

Table 6. Final 3 × 3 Parametric Study 22

Table 7. Effect of Particle Size and Solid Loading on Fractional Concentration of Ce(III) 45

LIST OF FIGURES

Page

Figure 1. 3D structure of ceria (ICDD PDF 00-004-0593)[6]. 2

Figure 2. Schematic of the Lithoz LCM system[24]. 6

Figure 3. TGA measurement for an alumina green part: weight (solid line), weight change (dotted line)[23]. 7

Figure 4. Hot shrinkage of ceria[23]. 8

Figure 5. Failed initial test print with delaminated layers. 12

Figure 6. Preconditioned, 1 µm powder, medium solid loaded ceria samples. 13

Figure 7. XRD data of 0.5, 1, 2, and 10 µm advertised CeO_2 powders. 18

Figure 8. Grindometer measurement of (a) 10 µm powder and (b) 2 µm powder. 20

Figure 9. SEM image of agglomerates in 10 µm powder. 21

Figure 10. BET measurements of calcined 10 µm powder. 21

Figure 11. Effect of particle size on bulk density of CeO_2, sintered at 1100˚C. 23

Figure 12. Effect of particle size on bulk density of CeO_2, sintered at 1450˚C. 23

Figure 13. Effect of particle size on bulk density of CeO_2, sintered at 1650˚C. 24

Figure 14. Effect of sintering temperature on bulk density of CeO_2, 0.5 µm particle size. 25

Figure 15. Effect of sintering temperature on bulk density of CeO_2, 1 µm particle size.. 25

Figure 16. Effect of sintering temperature on bulk density of CeO_2, 2 µm particle size.. 26

Figure 17. Effect of solid loading on bulk density of CeO_2, 0.5 µm particle size. 27

Figure 18. Effect of solid loading on bulk density of CeO_2, 1 µm particle size. 27

Figure 19. Effect of solid loading on bulk density of CeO_2, 2 µm particle size. 28

Figure 20. Samples printed with 39 vol%, 1 µm particle size powder, (a) top view, (b) cross section view, (c) edge interface view of sample sintered at 1100°C; (d) top view, (e) cross section view, (f) edge interface view of sample sintered at 1450°C; (g) top view, (h) cross section view, (i) edge interface view of sample sintered at 1650°C. 29

Figure 21. Samples printed with 41.5 vol%, 2 µm particle size powder, (a) top view, (b) cross section view, (c) edge interface view of sample sintered at 1100°C; (d) top view, (e) cross section view, (f) edge interface view of sample sintered at 1450°C; (g) top view, (h) cross section view, (i) edge interface view of sample sintered at 1650°C. 30

Figure 22. Samples printed with 39 vol%, 0.5 µm particle size powder, (a) top view, (b) cross section view, (c) edge interface view of sample sintered at 1100°C; (d) top view, (e) cross section view, (f) edge interface view of sample sintered at 1450°C; (g) top view, (h) cross section view, (i) edge interface view of sample sintered at 1650°C. 31

Figure 23. Samples printed with 37 vol%, 1 µm particle size powder, (a) top view, (b) cross section view, (c) edge interface view of sample sintered at 1100°C; (d) top view, (e) cross section view, (f) edge interface view of sample sintered at 1450°C; (g) top view, (h) cross section view, (i) edge interface view of sample sintered at 1650°C. 32

Figure 24. Samples printed with 39.4 vol%, 2 µm particle size powder, (a) top view, (b) cross section view of sample sintered at 1100°C; (c) top view, (d) cross section view, (e) edge interface view of sample sintered at 1450°C; (f) top view, (g) cross section view, (h) edge interface view of sample sintered at 1650°C. 33

Figure 25. Samples printed with 37 vol%, 0.5 µm particle size powder, (a) top view, (b) cross section view, (c) edge interface view of sample sintered at 1100°C; (d) top view, (e) cross section view, (f) edge interface view of sample sintered at 1450°C; (g) top view, (h) cross section view, (i) edge interface view of sample sintered at 1650°C. 34

Figure 26. Samples printed with 41 vol%, 1 µm particle size powder, (a) top view, (b) cross section view, (c) edge interface view of sample sintered at 1100°C; (d) top view, (e) cross section view, (f) edge interface view of sample sintered at 1450°C; (g) top view, (h) cross section view, (i) edge interface view of sample sintered at 1650°C. 35

Figure 27. Samples printed with 43.4 vol%, 2 µm particle size powder, (a) top view, (b) cross section view, (c) edge interface view of sample sintered at 1100°C; (d) top view, (e) cross section view, (f) edge interface view of sample sintered at 1450°C; (g) top view, (h) cross section view, (i) edge interface view of sample sintered at 1650°C. 36

Figure 28. Samples printed with 41 vol%, 0.5 µm particle size powder, (a) top view, (b) cross section view, (c) edge interface view of sample sintered at 1100°C; (d) top view, (e) cross section view, (f) edge interface view of sample sintered at 1450°C; (g) top view, (h) cross section view, (i) edge interface view of sample sintered at 1650°C. 37

Figure 29. Sample pressed with 0.5 µm particle size powder and sintered at (a) 1100°C, (b) 1450°C, and (c) 1650°C; sample pressed with 1 µm particle size powder and sintered at (d) 1100°C, (e) 1450°C, and (f) 1650°C; sample pressed with 2 µm particle size powder and sintered at (g) 1100°C, (h) 1450°C, and (i) 1650°C. 38

Figure 30. Effect of sintering temperature on the microstructure of CeO_2, 1 µm particle size, high solid loading; Sample sintered at (a) 1100°C, (b) 1450°C (b), and (c) 1650°C. 39

Figure 31. Effect of particle size on the microstructure of CeO_2, sintered at 1450°C, medium solid loading; (a) Sample printed with 1 µm particle size powder, (b) Sample printed with 2 µm particle size powder, and (c) Sample printed with 0.5 µm particle size powder. 40

Figure 32. Effect of particle size on grain size of CeO_2, sintered at 1100°C. 41

Figure 33. Effect of solid loading on grain size of CeO_2, 1 µm particle size. 42

Figure 34. Effect of sintering temperature on grain size of CeO_2, medium solid loading. 42

Figure 35. XPS spectra of all 9 measured samples. 43

Figure 36. XPS spectra and fitted peaks for sample with 41 vol% solid loading and 0.5 µm particle size powder. 44

Figure 37. Layering effect on internal microstructure, 0.5 µm particle size, medium solid loading. 45

Figure 38. SEM micrograph of printed ceria sample (a) cross section-edge interface, (b) delamination between printed layers. 46

Figure 39. SEM micrographs of (a) top surface of printed ceria sample with pitting, (b) bottom surface of printed ceria sample without pitting. 47

Figure 40. Image of convexity on sample surface. 48

ABSTRACT

Additive manufacturing enables freedom of design and rapid prototyping which are valuable assets in every application and industry. Cerium oxide (ceria) is well-known for applications in various fields, including abrasives, electro ceramics, and medicine, and understanding the working mechanisms of lithography-based manufacturing of ceria will help advance the technology in these fields. This investigation was focused on the effects of modulating process parameters for additive manufacturing of ceria ceramics with a CeraFab 8500, lithography-based 3D printer. A 3 × 3 parametric study was designed with intentions of mapping the effects of process parameter alterations of 3D printed ceria parts. Characteristics such as grain size, porosity, stoichiometry, and density were used to compare printed samples with traditionally processed and sintered ceria. Main parameters varied were powder particle size, solid loading of the photocurable slurry, and sintering temperature, with each having a low, medium, and high value.

Ceria powders with a particle size of 0.5 μm and slurry solid loading of 41.5 vol% produced high-density ceramics with complex structures and geometries. A maximum sintered density of 98.3% of theoretical was achieved with no apparent porosity. The optimal sintering temperature was found to be ~ 1450°C and x-ray photoelectron spectroscopy results showed no significant variation of Ce(III) concentration between the printed samples.

I. INTRODUCTION

Cerium oxide (CeO_2, Ceria) is widely used in various applications and industries including electroceramics[1], surface polishing[2], solid state electrochemistry[3], and nanomedicine[4]. Ceria has been used as a model system for metal oxide electrolytes with a fluorite crystal structure. Materials like zirconia, for example, need stabilization into a cubic structure via doping with calcium, magnesium, or yttrium oxide, where ceria does not. In addition, with a higher ionic conductivity than that of zirconia, ceria is attractive for solid oxide electrolyte applications. Various microstructural parameters and the thermal treatment of ceria samples produce a large effect on electrical and mechanical properties.

The focus of this study is to investigate the printability of ceria with a lithography based ceramic manufacturing (LCM) 3D printer to produce dense ceramics. The Lithoz CeraFab 8500 was used to print pure ceria samples with a range of densities and microstructures. A parametric study was designed and used to investigate the sensitivity of several process parameters on the overall printability of ceria and the quality of the printed parts. Grain size, porosity, density, and microstructure of the samples were used to compare them and determine the effects of the process parameters. In addition, hydrostatically uniaxially pressed ceria pellets were prepared and used for comparisons between 3D-printed samples and traditionally processed samples. The variables in the study were the ceramic powder particle size, solid loading of the printable slurry, and sintering temperature. Each parameter was varied at three levels spanning the expected workable range for that variable. The process window of the CeraFab 8500 was determined and the working mechanisms for the printability were presented. A recommendation for optimum process parameters was made based on the effect and sensitivity of each variable in the study.

II. LITERATURE REVIEW

A. Material Background

Cerium, with an atomic number of 58 and an electronic configuration of $[Xe]4f^15d^16s^2$, has a variable electronic structure, meaning the relative occupancy of electronic levels can be changed with a small amount of input energy[5]. This allows cerium to exist naturally in the Ce^{3+} and the Ce^{4+} states, giving the element its dual valence states. Cerium oxide, also commonly known as ceria, ceric oxide, or cerium dioxide, is a rare earth metal oxide. Ceria forms a classic cubic fluorite structure and in its bulk form is diamagnetic (Figure 1)[6]. Ceria is catalytically active due to its ability to easily change ionic states[7]. Ceria is also known to have very high absorption in the UV range, therefore, it is used in the medical and cosmetic industries[8]. Due to its high ionic conductivity, low activation energy, and low cost, ceria is commonly used as a catalyst in solid oxide fuel cells (SOFCs)[9]. Nanocrystalline as well as doped ceria have been extensively investigated for SOFC applications as an electrolyte[10-14].

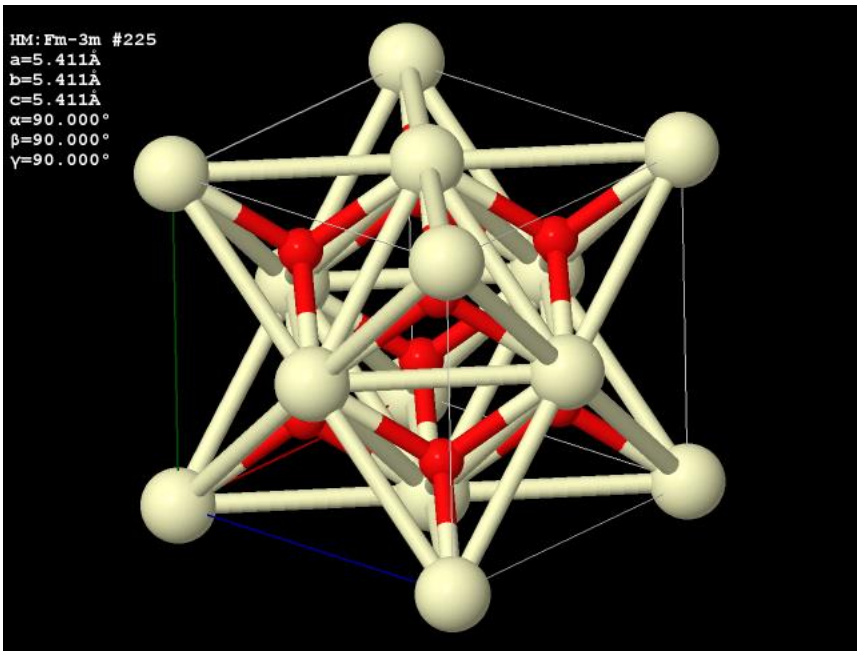

Figure 1. 3D structure of ceria (ICDD PDF 00-004-0593)[6].

Many studies have been carried out, which investigate the oxidation state of cerium within ceria using x-ray photoelectron spectroscopy (XPS). Variations in sintering

schedules, as well as the addition of dopants, such as gadolinium have been known to affect the reduction of ceria[12, 15-17]. It has been found that an XPS spectrum of Ce_{3d} in CeO_{2-y} will show 10 peaks, depending on the concentrations of Ce(III) and Ce(IV). Quantitative analysis of this spectra can be used to measure the fractional concentrations of Ce(III) and Ce(IV). XPS results do not directly measure the concentration, however, a Laplace transform of the actual concentration of the surface of the material. Table 1 shows the binding energies and the corresponding origin ion for Ce $3d_{5/2}$ and Ce $3d_{3/2}$ CeO_{2-x}[18].

Table 1. Reference XPS BE Peaks for Ce $3d_{5/2}$ and Ce $3d_{3/2}$[18]

		V_o	V	V'	V''	V'''
Ce $3d_{5/2}$	Origin	Ce^{3+}	Ce^{4+}	Ce^{3+}	Ce^{4+}	Ce^{4+}
	BE (eV)	880.6	882.6	886.7	888.85	898.4
		u_o	U	u'	u''	u'''
Ce $3d_{3/2}$	Origin	Ce^{3+}	Ce^{4+}	Ce^{3+}	Ce^{4+}	Ce^{4+}
	BE (eV)	898.9	901.05	903.05	907.45	916.7

B. Additive Manufacturing of Ceramics

Complex ceramic geometries are difficult to produce in comparison to metals and polymers[19]. Where metals and polymers can be easily machined to achieve appropriate geometry, tolerance and surface finish, machining ceramics is no small task. Additive manufacturing (AM) has come a long way in terms of range of materials, technology, and consumer availability, however notably, ceramics have been lagging in comparison to other materials (Table 2). As the physical properties of ceramics are so sensitively dependent on flaws such as cracking, porosity, homogeneity, and crystalline defects, the margin for error with ceramic processing techniques and technology is very narrow[20].

Table 2. AM Processes[21]

Process	Laser-based?	Materials
Powder bed fusion	Yes	Metal, Polymer, Ceramic
Direct energy deposition	Yes	Metal
Vat polymerization	Yes	Metal, Polymer, Ceramic
Sheet lamination	Can be	Metal, Polymer, Ceramic
Binder jetting	No	Metal, Polymer, Ceramic
Material jetting	No	Polymer
Material extrusion	No	Polymer

Recent advances in AM have led to a range of techniques that all produce reliable ceramics for their niche applications. These processes include stereolithography (SLA), direct writing (DW), robotic material extrusion, and powder bed fusion (PBF). Wet slurry- as well as dry powder-fed systems have been developed. In most AM systems for ceramics, a post processing step is required to densify the printed ceramic parts. The systems differ in how the printed parts are bound, prior to densification.

Wet slurry-fed AM systems including SLA and robotic material extrusion are all similar in that they use a wet slurry as the feedstock. Wet slurries are a homogenous mixture of a type of binder system, dispersants, and additives, with a suspension of ceramic powder. SLA printing uses a rastering laser beam to selectively cure a polymer binder. This solid polymer matrix binds the ceramic powder before being burned out and the ceramic can be sintered. Robotic material extrusion uses a wet slurry extrusion to layer by layer construct a desired geometry. The wet slurry in an extrusion-based printing technique is cured, usually thermally, during the printing process. Critical process dependent variables for wet slurry systems include the rheology of the slurry, solid loading of ceramic powder in the slurry, optical properties of the powder, and the physical dimensions and geometry of the powder particles.

PBF and binder jetting are AM techniques that utilizes a dry powder as the feedstock. The powder can be a range of materials including metals or ceramic. PBF uses a laser to selectively melt the powder. The laser beam rasters a two-dimensional (2D) cross section view of the desired part on a thin layer of the feed powder. The next thin layer of powder is then spread over the solidified layer and the subsequent layers are then solidified. The binder jetting system has a similar powder bed and powder spreading mechanism,

however, it differs as the laser is replaced by a printhead that extrudes a liquid binder to solidify the powders. The binder must be burned off and the powders sintered in post-processing.

C. Lithoz LCM Process

Digital light projection (DLP) stereolithography has long been used for AM of ceramics. Advancements in optics and image projection have allowed this system to give very high lateral resolution while also keeping processing time down when compared to a similar power SLA rastering laser system.

The Lithoz system employs a lithography-based ceramic manufacturing (LCM) technique that utilizes a liquid-based photosensitive slurry to produce three-dimensional parts[19]. The LCM technique is designed to efficiently print with high viscosity materials, like a ceramic suspension. LCM is a subset of DLP stereolithography that has been patented for the proprietary Lithoz GmbH binder systems[22]. The liquid-based slurry is comprised of a photosensitive resin and a suspension of ceramic powder. The photosensitive resin is a mixture of photoinitiators, low molecular weight monomers, and dispersants. The resin follows a photopolymerization reaction to bind the ceramic powders to form a green body. A combination of a light-emitting diode (LED) array and a digital micromirror device (DMD) are used to selectively polymerize the resin. This light engine, in addition to its dedicated projection optics, produces near uniform light intensity throughout the build area. There is generally an intensity drop of 1.6% between the center of the build area and the corners. Light exposure on the liquid slurry excites the photoinitiators to start the photopolymerization. The excited photoinitiator undergoes a reaction to produce either type I or type II photoinitiators, also called radicals. These radicals then consume the low molecular weight monomers to produce long polymer chains and ultimately solidifying the slurry into a polymer network[23].

A build plate is held upside down in the print envelope with a circular vat placed below it, as shown in Figure 2. The photosensitive slurry is placed in the vat prior to beginning the print process. To begin the print, the build plate is lowered onto the vat and pressed uniformly into the slurry. A light engine below the clear vat projects a 2D cross section of the desired part up into the slurry to initiate the photopolymerization reaction.

This binds the solidified layer onto the build plate. The build plate is then raised out of the vat to allow a wiper blade to recoat and level the slurry in the vat. With the vat recoated, the build plate can move back down into the vat and start the cycle again.

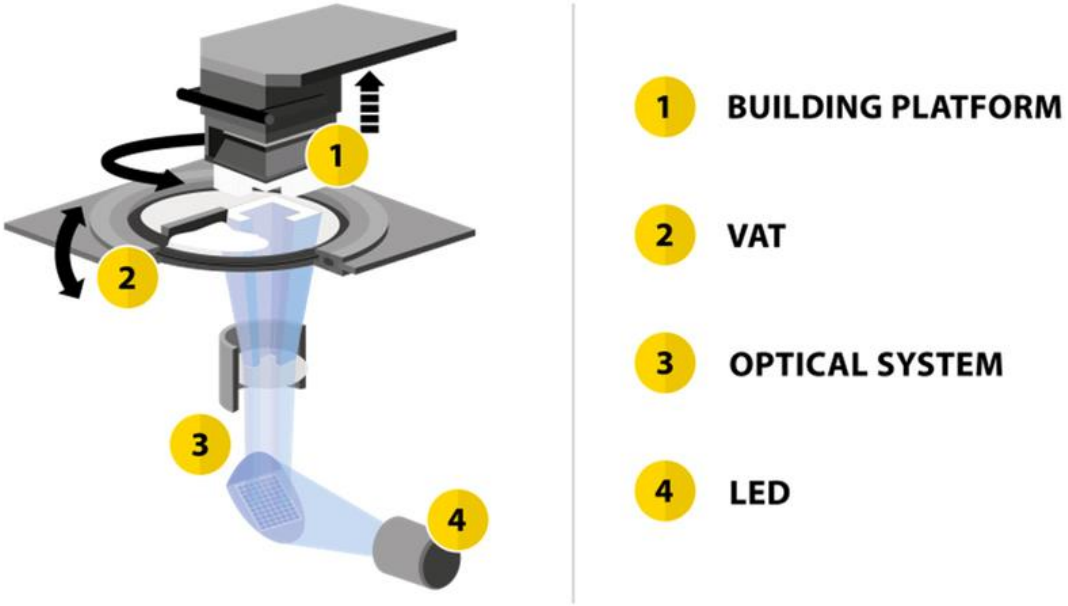

Figure 2. Schematic of the Lithoz LCM system[24].

As the produced green body is comprised of a polymer matrix binding the ceramic powder, a subsequent post-processing schedule is required to debind and densify the 3D-printed ceramic parts. Immediately following printing, the parts must be preconditioned. The preconditioning stage consists of a slow ramp up to 120˚C with intermittent isothermal dwell periods. Preconditioning must be completed before the parts can be handled and stored for an extended period of time. A slow ramp up to 1100˚C and intermittent isothermal dwell periods make up the debinding stage. This breaks down and off-gases the polymer matrix to leave a pure ceramic body. Thermogravimetric analysis (TGA) and differential scanning calorimetry (DSC) of printed parts show the decomposition and weight loss due to the debinding of the polymer matrix (Figure 3). Hold points and reduced heating rates are used in the regions of high decomposition rate to allow for complete decomposition and burn out[23]. The debinding stage also induces a slight coalescing effect in the ceramic powder to help hold the structure together between debinding and sintering

stages. Following a debinding stage, the ceramic body is ready for densification. A ramp up to the specific materials sintering temperature with intermittent isothermal dwell periods as well as at the maximum temperature make up the sintering stage.

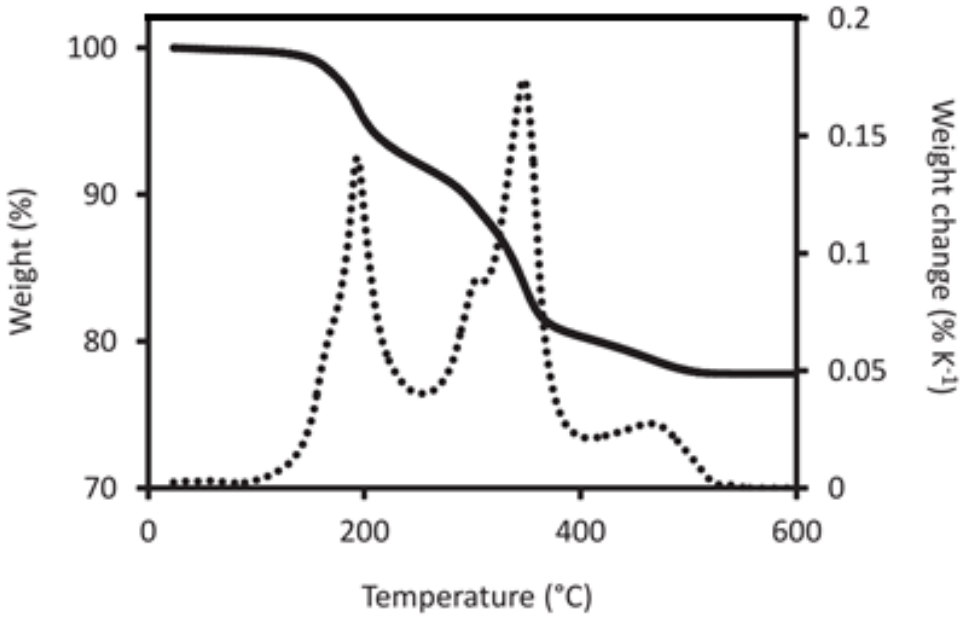

Figure 3. TGA measurement for an alumina green part: weight (solid line), weight change (dotted line)[23].

D. Ceria Sintering

Ceria is known to be one of the highest refractory oxides with a melting point of 2750˚C. The sintering behavior of ceria has been extensively investigated with the effects of powder particle size[25], hot pressing, cold sintering[26], as well as the addition of a range of dopants for conductivity optimization[1, 12, 16, 17, 27] and controlling densification behavior[28].

As the powder particle size has a large effect on the quality and reproducibility of AM produced ceramics, the effects of particle size on the densification and grain growth behavior of ceria were of interest. F. A. Akopov *et.al.*[25] studied how the densification of ceria was affected by finely grinding a powder. The smaller particle size powders sintered to the same bulk density as large powders but at a reduced temperature. Sintering of pressed

ceria pellets begins ~ 1100°C and densification takes place significantly over ~ 1300 - 1500°C. Figure 4 shows the shrinkage of a ceria pellet up to 1600°C.

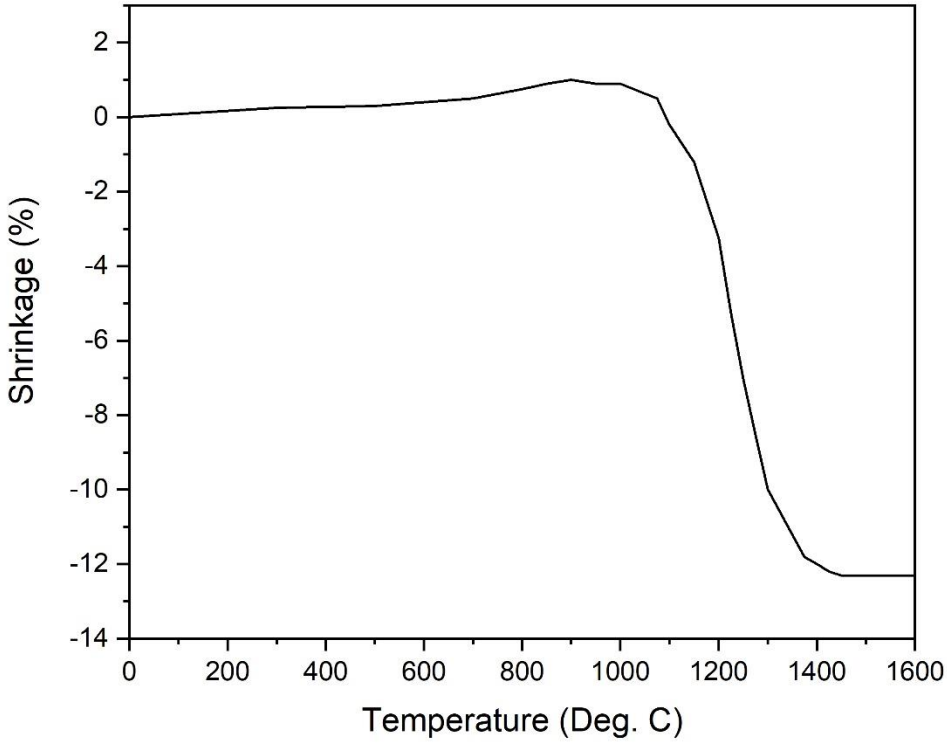

Figure 4. Hot shrinkage of ceria[23].

III. EXPERIMENTAL PROCEDURE

A. Parametric Study

Powder particle size was the first parameter to be populated into the parametric study. The criteria for selecting powders included a minimum purity of 99.95% and all three particle sizes were to be sourced from the same supplier. This is to help reduce the possibility of variations in particle geometry and purity caused by differences in powder production methods. The particle sizes would also range from on the order of 100s nm - 10s μm. Advanced Abrasives Corporation supplied ceria powders with advertised purity of 99.95% and advertised particle sizes of 0.5 μm, 1 μm, 2 μm, and 10 μm (Advanced Abrasives Corporation, Pennsauken, NJ). A 2 kg batch of each particle size was purchased, allowing for 1 kg to be used for powder characterization and producing pressed pellets for comparison purposes, and 1 kg to be used for slurry development and printed samples.

Following particle size selection, values for the sintering temperatures and solid loadings were chosen. The methodology for the solid loading selection was based purely on the rheology and predicted printability of the slurry. Maximum solid loading depends on the viscosity of the developed slurry. As particle size has a direct effect on the slurry viscosity, the vol% value is not held constant between each particle size, rather the solid loading was compared with respect to the rheology of the slurry. As the quality of the printed part positively correlates with the solid loading of the slurry, the maximum solids loaded slurry that was deemed workable in the LCM system was chosen as the medium value for the parametric study. The low and high values were then chosen as the expected low and high bounds of the processing window.

Finally, sintering temperatures were determined with a simple sintering test of five pressed ceria pellets, which were each sintered at increasing temperatures between 1400°C and 1600°C. Density and porosity of each pellet were measured using the immersion method (American Society for Testing Methods standard C20-00) and grain growth, using scanning electron microscopy (SEM, FEI™ Quanta 200F, FEI Company, Hillsboro, OR) micrographs in ImageJ image processing and analysis software. The highest density pellet with the least amount of grain growth was selected as the medium sintering temperature. The low sintering temperature was chosen as the maximum temperature achieved in the

debinding schedule. The debinding stage caused a slight coalescing of the powder particles to allow the structure to hold its shape between the debinding and sintering stages. The early coalescing of the particles was expected to produce a very low-density solid part. The high sintering temperature was chosen because of the grain growth effect that was seen in the sintering test pressed pellets. This was expected to produce a high-density part with uniform grains and low porosity. The optimal sintering temperature was found to be 1450°C, the high sintering temperature value of 1650°C and the low sintering temperature was found to be 1100°C.

B. Powder Characterization

The raw sourced ceramic powder was characterized to confirm phase, purity, and particle geometry. Density, particle size, x-ray diffraction (XRD), and scanning electron microscopy (SEM) were used for characterization of the powders used in the study. Particle size measurements were used to compare actual particle size to the advertised particle sizes from the supplier. XRD diffractograms were taken in order to confirm the phase and purity of the material. SEM micrographs were taken to examine the particle geometry and any agglomeration in the raw powders.

Density measurements were made using a helium pycnometer (AccuPyc II 1340, Micromeritics, Norcross, GA). The AccuPyc II system uses gas displacement as means to accurately measure sample volume for irregular geometries. Helium is used as the displacement gas and samples containing surface roughness, porosity, and small fractures as small as one angstrom can be measured. The powders were dried overnight in a drying oven at 110°C before being placed in the pycnometer sample container. Five measurements were taken for each powder batch and the results were averaged.

XRD was used to confirm the phase of the sourced powders (D2 Phaser, Bruker AXS, Inc., Madison, WI). The powders were dried overnight in a drying oven held at 120°C before being lightly pressed into the Bruker sample trays. The measurements were taken with a 2Θ range of 5° through 80°. The patterns were then baseline-corrected, and peaks indexed in OriginLab 2020. Ceria holds a cubic fluorite structure with pronounced peaks in the (111), (200), (220), (331), (222), (400), and (420) planes.

Actual particle size was also measured. The measurements were compared to the advertised sizes and also show the standard deviation for each powder batch. The powders were analyzed by sedimentation to find actual particle size (SediGraph III PLUS, Micromeritics, Norcross, GA). Each batch of powder was held in a drying oven overnight prior to being measured. The powders were suspended in a mixture of deionized water and Darvan C. The mixture was 0.25% ceria powder by mass and 2 drops of Darvan C was used as a dispersant. Prior to running the ceria suspension in the SediGraph, the mixture was held in an ultrasonic homogenizer to break up loose agglomerates (VCX 750, Sonics & Materials Inc., Newtown, CT).

C. Slurry Development

Slurry development was completed at Lithoz America LLC (Troy, NY, USA). A batch of 1 kg of each advertised particle size powder was supplied to Lithoz America for slurry development. The methodology for slurry development included completing grindometer (1256865, BYK-Gardner, Geretsried, Germany) measurements for each slurry formulation to find large particles and agglomerates in the slurry. Each particle size batch was mixed with a proprietary binder system and the rheology was tracked as the solid loading was increased. Once the slurry reached a loading which caused significant shear thickening, the slurry was deemed unusable. The maximum loading, prior to shear thickening behavior, was used as the medium value for the parametric study. An increase of 2 vol% and a decrease of 2 vol% were used for the high and low values for the parametric study, respectively.

D. Printing Procedure

A print schedule was prepared to organize the print runs and optimize for printing time. Each print consisted of six, 0.5 cm diameter by 0.25 cm tall, cylinders. Following 3D-printing, the six parts were separated into 3 pairs and each pair was post processed together. This would produce two samples for each combination of the variables in the parametric study. Initial samples were printed following print parameters based on a similar slurry formulation for alumina. This print run was completed at an ambient temperature of

22°C. Delamination between layers caused the cylinder to morph into a structure with sharp peaks and valleys (Figure 5).

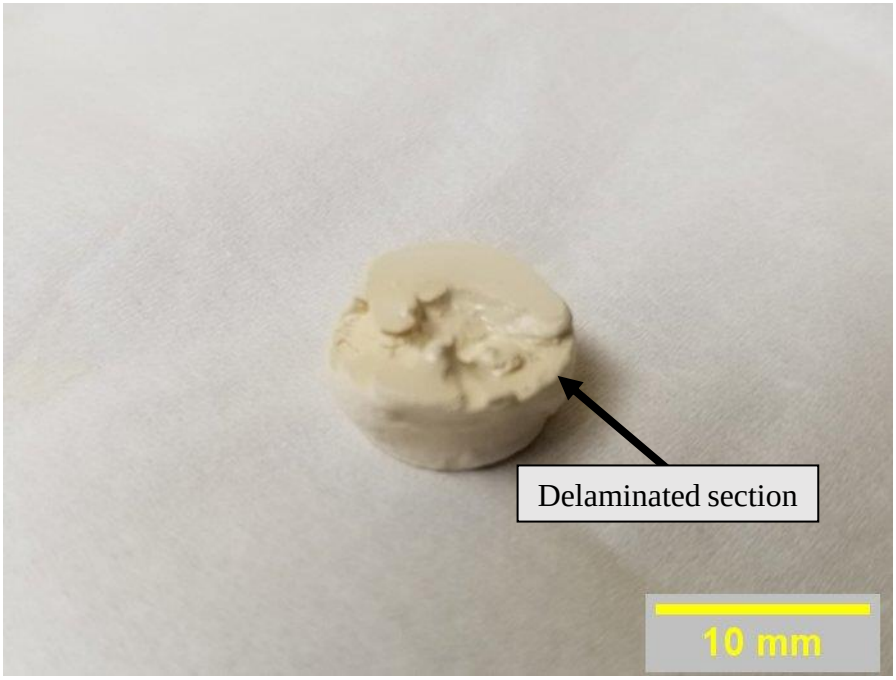

Figure 5. Failed initial test print with delaminated layers.

A slurry with a high viscosity or shear thickening behavior will produce an uneven surface when the slurry is recoated between layers. The uneven slurry surface gives poor contact between the uncured slurry and the cured part. Poor contact introduces bubbles and gaps between layers.

During the printing, the cured slurry that did not adhere to the part remained on the vat surface which caused the print vat surface to press strongly against the printed part when the build plate was lowered for each layer. As the vat surface was a flexible silicon film, the part being pressed on the vat caused the projected light to refract past the edge of the designed part cross section. This produced a cylinder that gradually became wider as the printing progressed.

Following the unsuccessful initial prints, changes were made to the printing process to produce a consistent solid part. This included the addition of a 100 W heater and temperature controller inside the print envelope. The addition of the heater helped reduce

the viscosity of the slurry. Sample printing continued at a raised ambient temperature of 29.5°C. The higher temperature allowed the slurry to be coated more evenly and to consistently produce high quality parts. Pre-sintered, green bodies of the successfully printed samples are shown in Figure 6.

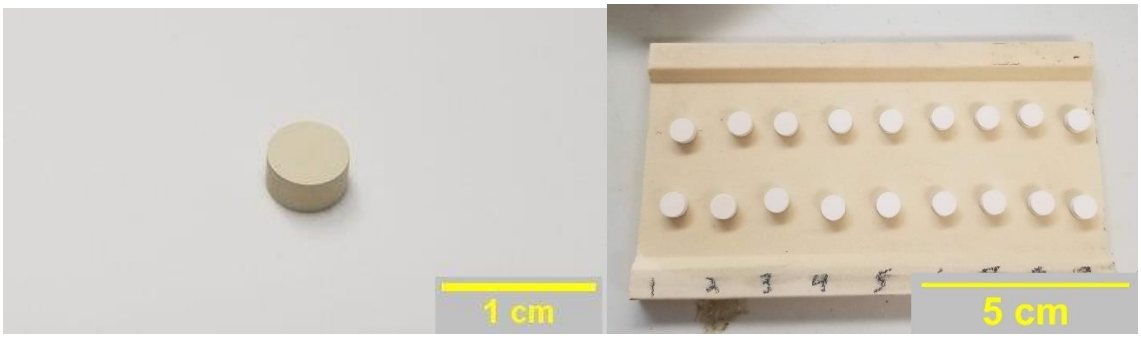

Figure 6. Preconditioned, 1 μm powder, medium solid loaded ceria samples.

Immediately following printing, the parts were preconditioned, debinded, and sintered per the supplied preconditioning, debinding, and sintering schedules as shown in Table 3.

Table 3. (a) CeO_2 Preconditioning Schedule, (b) CeO_2 Debinding Schedule, and (c) CeO_2 Sintering Schedule

(a)

Heating Time (h)	**Heating Rate (K/hr)**	**Temperature (°C)**	**Dwell Time (h)**
8.33	6	75	6
10.00	1	85	7
10.00	1	95	9
5.00	1	100	11
5.00	1	105	11
5.00	1	110	4
0.50	4	112	4
0.50	4	114	6
0.50	4	116	6
0.50	4	118	6
0.50	4	120	20
3.96	24	25	n/a

(b)

Heating Time (h)	**Heating Rate (K/hr)**	**Temperature (°C)**	**Dwell Time (h)**
3.28	28.9	120	1
1.67	6	130	4
6.67	6	170	4
8.33	6	220	4
5.00	6	250	6
12.50	6	325	6
8.75	12	430	2
3.09	55	600	0
9.09	55	1100	0
2.08	240	600	0
0.95	600	30	n/a

(c)

Heating Time (h)	**Heating Rate (K/min)**	**Temperature (°C)**	**Dwell Time (h)**
3.13	2	400	0
3.67	5	*	3
1.23	20	20	n/a

*Maximum sintering temperature is dependent on the parametric study

E. Bulk and Surface Characterization

Density was measured using the Archimedes immersion method. American Standards and Testing Methods (ASTM) standard C20-00 was followed. The samples were dried in a drying oven overnight then weighed on a 4 decimal scale (OHAUS Analytical Plus, OHAUS Corporation, Parsippany, NJ). After the dry weights were taken, the samples were boiled in DI water for 2 hours. Following the 2 h boil, the heat was turned off and the samples were left submerged overnight. The samples were then weighed while submerged and also weighed after being blotted on a damp paper towel to remove all excess water droplets. Density, pore volume and porosity were then calculated using the following equations:

$$Density = \frac{D}{W - S} * \rho water \quad (1)$$

$$Pore\ Volume = (W - D) * \rho water \quad (2)$$

$$Porosity = \frac{W - D}{W - S} * \rho water * 100 \quad (3)$$

where, D is the dry weight, W is the saturated weight after being blotted, S is the weight of the submerged suspended weight, and ρ is the density of water, assumed to be 0.9975 g/cm^3. In addition to measuring the density, SEM micrographs were used to analyze the microstructure of the printed samples. Images of the top surface were taken and used to find grain size of the samples. The rounded edges of the samples were then ground using 400 grit up to 1200 grit SiC abrasive paper in order to expose the cross section. The internal microstructure was then imaged, as well as images showing the layering and edge effects in the samples. Prior to imaging the samples, the samples were sputter-coated with gold in a coater (Model 108, Cressington Scientific Instruments, Watford, UK). The samples were attached to aluminum SEM stages with double sided carbon tape then gold coated for 40 seconds in a vacuum pressure of 0.06 bar. The samples were then moved directly into the SEM.

XPS was used to measure the fractional oxidation states of Ce in the samples sintered at a single sintering temperature. This investigated the effects of both particle size of the raw ceria powder and the solid loading of the slurry on the concentration of Ce(III) and Ce(IV) in the printed samples. XPS was performed using a PHI Quantera Scanning X-

Ray Photoelectron Microprobe, using monochromatic Al Kα x-rays (ULVAC-PHI Inc, Chanhassen, MN). Survey scans were performed, as well as spot scans of the Ce_{3d} peaks. The spectra were then compiled in Fityk data analysis software and the corresponding V_o, V, V', V'', V''', u_o, u, u' u'', and u''' peaks were fit to the spectra and the area under each peak curve was determined. Then, the fractional concentration of Ce(III) was calculated using the following equations:

$$Ce(III) = V_o + u_o + V + u' \quad (4)$$

$$Ce(IV) = V + V'' + V''' + u + u'' + u''' \quad (5)$$

$$[Ce(III)] = Ce(III)/[Ce(III) + Ce(IV)] \quad (6)$$

where Ce(III) and Ce(IV) are the summation of the integrated peak areas and [Ce(III)] is the fractional concentration of Ce(III) in the sample.

IV. RESULTS AND DISCUSSION

A. Powder Characterization

1. Powder Density

The measured density values are shown in Table 4. Theoretical density of CeO_2 used for calculations is assumed as 7.22 g/cm^3. The average measured density of each powder is 95.7 - 96.9% of theoretical densities. The low measured values are attributed to the closed porosity caused by agglomerations in the powders. SEM micrographs confirm a large amount of agglomeration in the raw powders.

Table 4. Density Measurements of 0.5, 1, 2, and 10 μm Advertised CeO_2 Powders

Sample	Advertised Particle Size (μm)	Sample Mass (g)	Average Density (g/cm^3)	Standard Deviation (+/-g/cm^2)
1	1	5.089	6.915	0.011
2	2	5.989	6.988	0.019
3	10	5.532	6.917	0.020
4	0.5	5.598	6.994	0.015

2. X-ray Diffraction (XRD)

Ceria has a cubic fluorite structure with pronounced peaks in the (111), (200), (220), (331), (222), (400), and (420) planes. All of which are identified in each XRD patterns collected for the sourced ceria powders. The XRD diffractograms for all 4 sourced powders are shown in Figure 7. Peak broadening from the smaller to the larger particle sizes indicated the average crystallite size correlated positively with particle size.

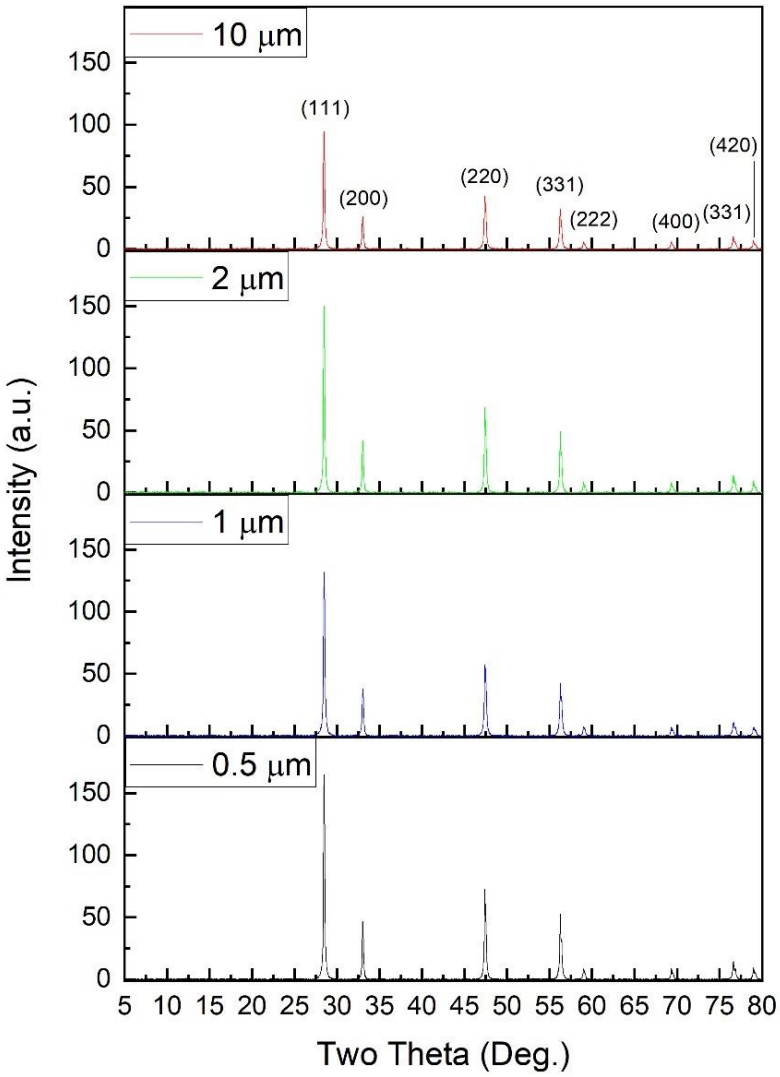

Figure 7. XRD data of 0.5, 1, 2, and 10 µm advertised CeO_2 powders.

3. Particle Size

The 0.5 µm, 2 µm, and 10 µm powders corresponded to measured particle sizes, 0.54 µm, 1.93 µm, and 9.73 µm respectively. However, the 1 µm advertised powder measured an average particle size of 2.00 µm. Initial SEM imaging suggested agglomerates in the 1 µm powder would cause larger than expected measured particle sizes but agglomerates in the other three advertised particle sizes would have caused a similar phenomenon. In addition, the ultrasonic homogenizer should have broken up the

agglomerates prior to the measurements being taken. Peak broadening in the XRD diffractogram also indicated the 1 μm powder had a larger average crystallite size than the 2 μm powder. Table 5 shows the actual particle size data.

Table 5. Powder Particle Size Measurements of 0.5, 1, 2, and 10 μm Advertised Powders

Advertised Particle Size (μm)	**Parameters (μm)**	**Test 1**	**Test 2**	**Test 3**	**Overall**
0.5	Measured Average Particle Size:	0.440	0.562	0.639	0.547
	Standard Deviation:	0.528	0.550	0.564	0.547
1	Measured Average Particle Size:	1.742	2.452	1.814	2.003
	Standard Deviation:	0.918	1.013	0.949	0.960
2	Measured Average Particle Size:	1.810	2.046	1.923	1.926
	Standard Deviation:	0.850	0.913	0.873	0.879
10	Measured Average Particle Size:	10.177	9.042	9.961	9.727
	Standard Deviation:	8.404	8.545	8.419	8.456

B. Slurry Development

All results presented under this section were completed by Lithoz America LLC (Troy, NY, USA). Maximum workable solid loading based on rheology of the slurry for the 0.5, 1, 2, and 10 μm powders were 39, 39, 41.5, and 20 vol%, respectively. The photosensitive slurry had a maximum curing depth of ~ 45 μm when loaded to a solid loading of 40 vol%. The high refractive index of ceria caused overpolymerization with printing light intensity > 300 mJ/cm^2. Self-polymerization was also exhibited by the slurry when stored at room temperature for periods of > 3 days. Based on these results, the middle solid loading was chosen as the maximum workable solid loading based on rheology and

the low and high solid loadings were –2 vol% and +2 vol%, respectively. It was recommended that the slurry be kept in cold storage to avoid self-polymerization, and the printing light intensity was lowered to 300 mJ/cm^2.

The 10 µm powder was chosen as the high value for particle size in the parametric study. The powder, along with the other three particle sizes were supplied to Lithoz America LLC for slurry development. Lithoz America was unable to produce a flowable slurry with a solid loading of > 20 vol%. The minimum solid loading for a workable slurry is ~ 40 vol% as shrinkage would cause cracking and delamination between layers during post-processing. Grindometer measurements showed large particles and agglomerates (> 50 µm) which produced the shear thickening behavior (Figure 8).

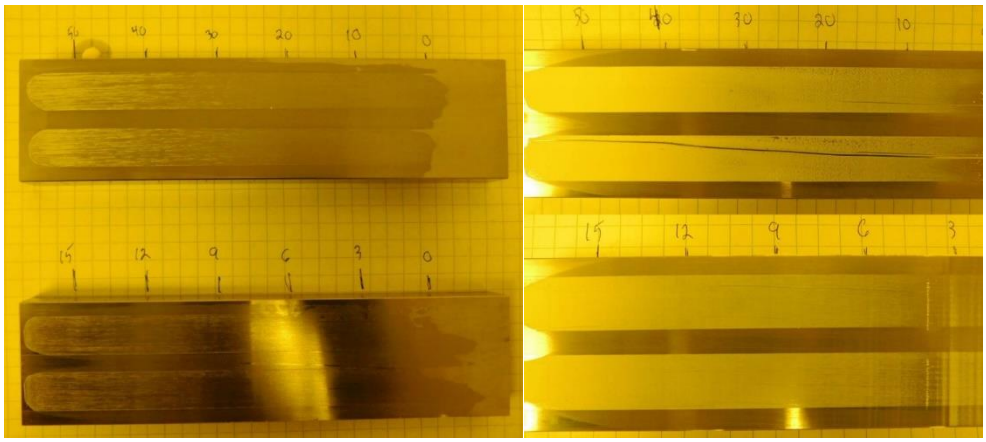

(a) (b)

Figure 8. Grindometer measurement of (a) 10 µm powder and (b) 2 µm powder.

Following this recommendation from Lithoz America regarding the 10 µm powder, SEM images were recorded for the 10 µm powder (Figure 9). As expected, very large agglomerates were found. The agglomeration in the powders was attributed to the high surface area geometry of the particles. Calcination was identified as a possible solution. This involved a thermal cycling of the 10 µm powder to reduce the surface area of the powder without beginning to coalesce the particles. To identify a suitable calcination temperature, a range of 600–700˚C was chosen from literature[29] and small batches of the 10 µm powder were heat-treated in a furnace at that temperature range. One batch each was heat-treated at 600˚C, 650˚C, and 700˚C. Brunauer–Emmett–Teller (BET) surface area was then measured for each batch of powder (Figure 10). By extrapolating the surface area

results, a temperature was found that would give a reduced surface area with no coalescing of the particles. The temperature of 850°C was selected and the results of calcining the 10 µm powder at 850°C is included in Figure 10. The calcined 10 µm powder was sent to Lithoz America for slurry development, however, development was still unsuccessful with the slurry having shear thickening behavior with a solid loading of ~30 vol%. The 10 µm powder was dropped from the study and proceeded with a 3 × 3 parametric study (Table 6).

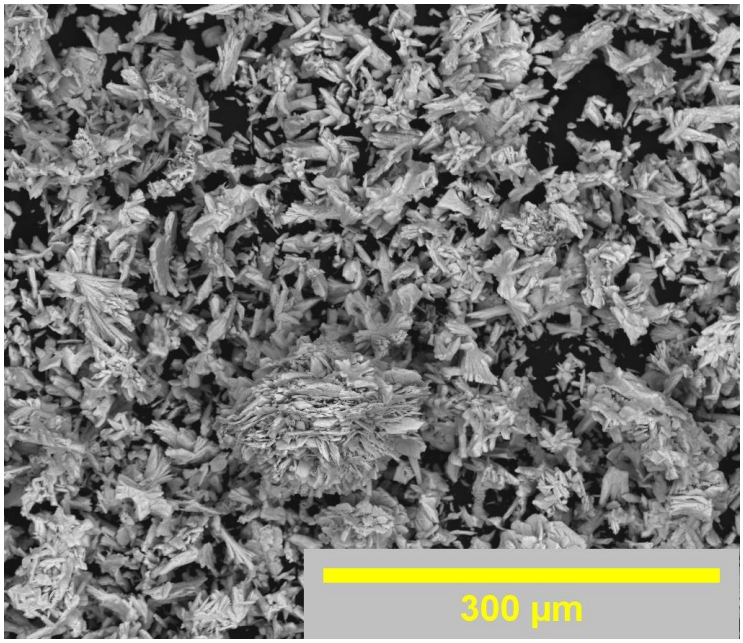

Figure 9. SEM image of agglomerates in 10 µm powder.

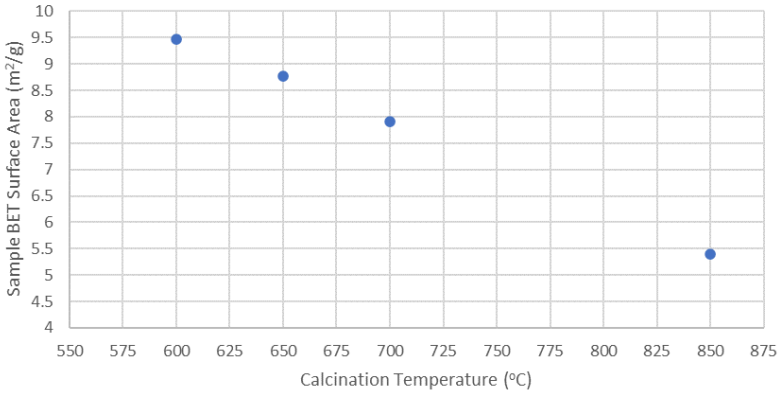

Figure 10. BET measurements of calcined 10 µm powder.

Table 6. Final 3 × 3 Parametric Study

Parameter	**Low**	**Medium**	**High**
Powder Particle Size	0.5 µm	1 µm	2 µm
Slurry Solid Loading	Low	Medium	High
Sintering Temperature	1100˚C	1450˚C	1650˚C

C. Printed Samples

Results of the printed samples included correlation of the density across the parametric study and investigating the effects on overall microstructure of the printed parts.

1. Bulk Density

a. Effect of Particle Size on Bulk Density

Figure 11-14 show the effect of particle size of powders on bulk density of printed parts. The samples were sintered at the sintering temperature of 1100˚C (Figure 11), 1450˚C (Figure 12), and 1650˚C (Figure 13). The bulk density for the pressed pellets was constant relative to varying particle size, however, jumped from ~ 5.8 g/cm^3 for parts sintered at 1450˚C up to ~ 7.0 g/cm^3 for parts sintered at 1650˚C. In every instance for the printed samples, the 0.5 µm particle size samples sintered to a higher density than the comparable 1 µm and 2 µm samples and the pressed samples were also of significantly higher density than the printed samples when sintered at the low sintering temperature of 1100˚C. The difference in density between the pressed and printed samples is due to the difference in packing density of the powder prior to sintering. The minimal difference between the density of the 1 µm and 2 µm powder samples also suggests the particle size measurements were accurate and the 1 µm advertised powder has an actual particle size of ~2 µm.

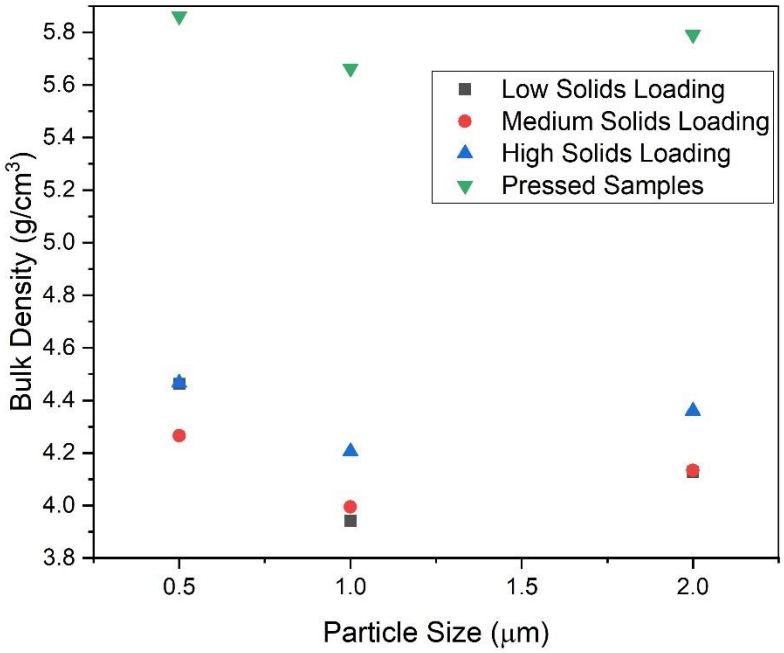

Figure 11. Effect of particle size on bulk density of CeO_2, sintered at 1100°C.

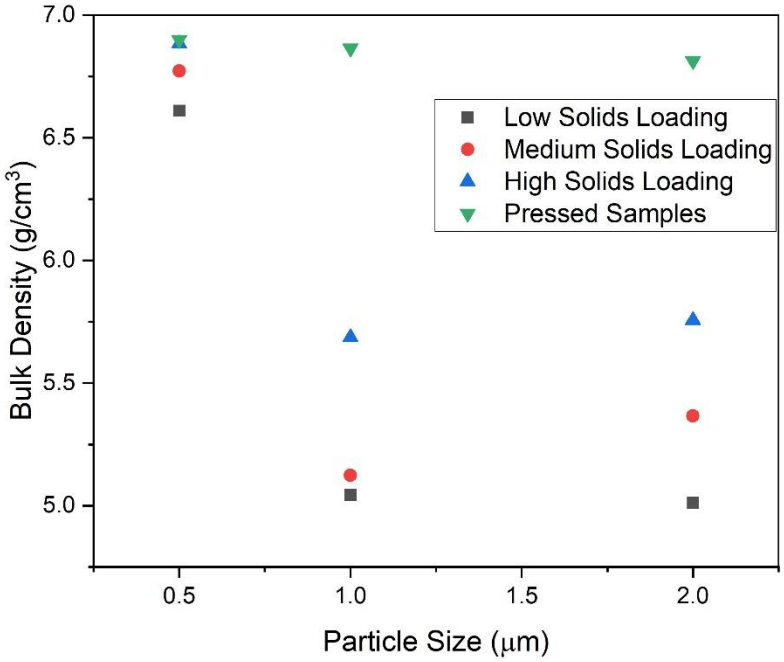

Figure 12. Effect of particle size on bulk density of CeO_2, sintered at 1450°C.

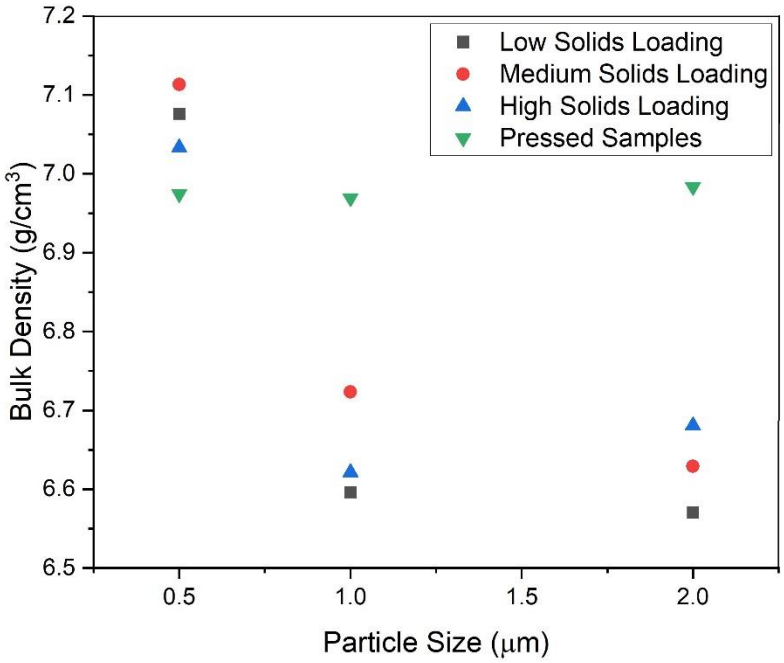

Figure 13. Effect of particle size on bulk density of CeO_2, sintered at 1650°C.

b. Effect of Sintering Temperature on Bulk Density

The effect of sintering temperature on bulk density is shown in Figure 14-17 corresponding to samples containing 0.5 µm, 1 µm, and 2 µm, respectively. The effect of sintering temperature on the samples stays consistent across each particle size. As expected, the bulk density correlates positively with sintering temperature. The 0.5 µm powder reached the highest bulk density at ~ 7.1 g/cm^3 and the 1 µm and 2 µm powder were slightly less dense at a maximum of ~ 6.7 g/cm^3. The 0.5 µm powder also showed a consistent density between each solid loading, including the pressed samples, when sintered at the medium and high temperatures. The 1 µm and 2 µm printed samples were all found to be less dense than the pressed samples, even at the highest sintering temperature of 1650°C.

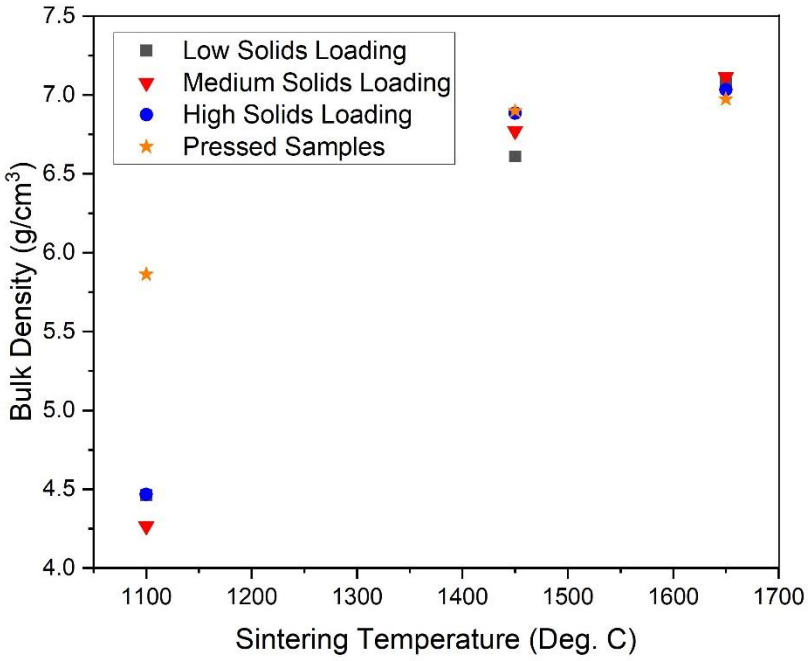

Figure 14. Effect of sintering temperature on bulk density of CeO_2, 0.5 µm particle size.

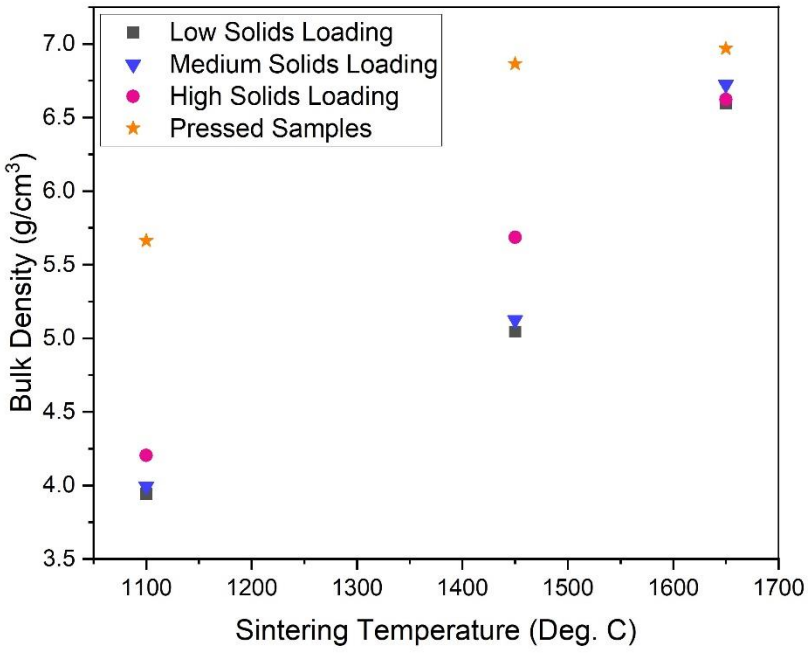

Figure 15. Effect of sintering temperature on bulk density of CeO_2, 1 µm particle size.

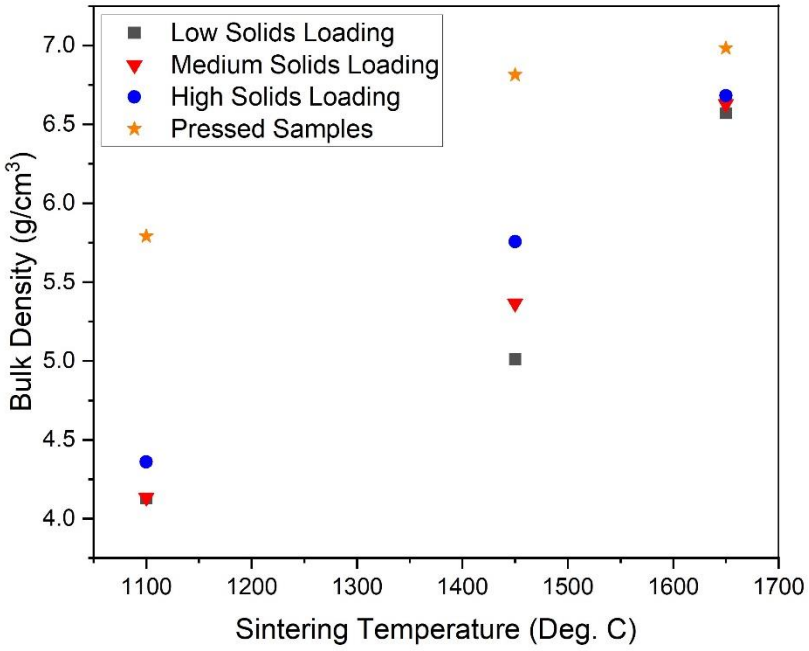

Figure 16. Effect of sintering temperature on bulk density of CeO_2, 2 µm particle size.

a. Effect of Solid Loading on Bulk Density

Solid loading of the slurry vs bulk density can be seen in Figure 17-20 for the 0.5 µm (Figure 17), 1 µm (Figure 18), and 2 µm (Figure 19). As in the case of previous comparisons, the 0.5 µm powder samples reached the maximum bulk density with the 1 µm and 2 µm powder samples ~ 0.6 g/cm^3 less dense. Solid loading has a minimal effect on the bulk density of the final sample. The density correlated slightly positive with the medium solid loading to the high but showed no significant effect from the low to the medium solid loading.

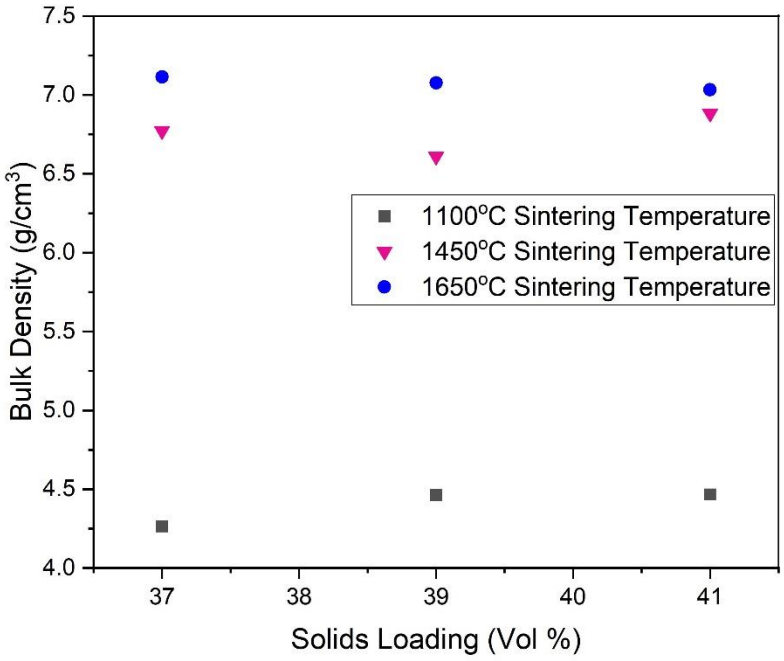

Figure 17. Effect of solid loading on bulk density of CeO_2, 0.5 µm particle size.

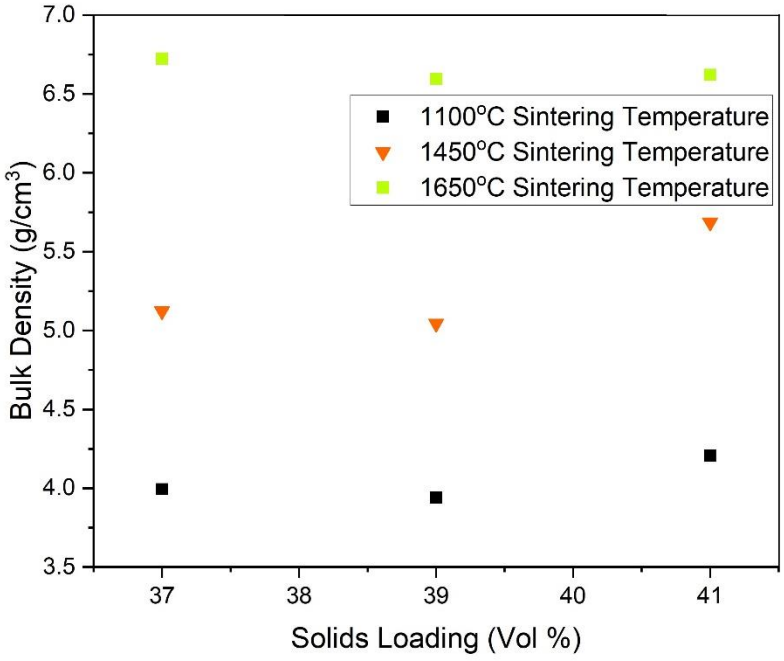

Figure 18. Effect of solid loading on bulk density of CeO_2, 1 µm particle size.

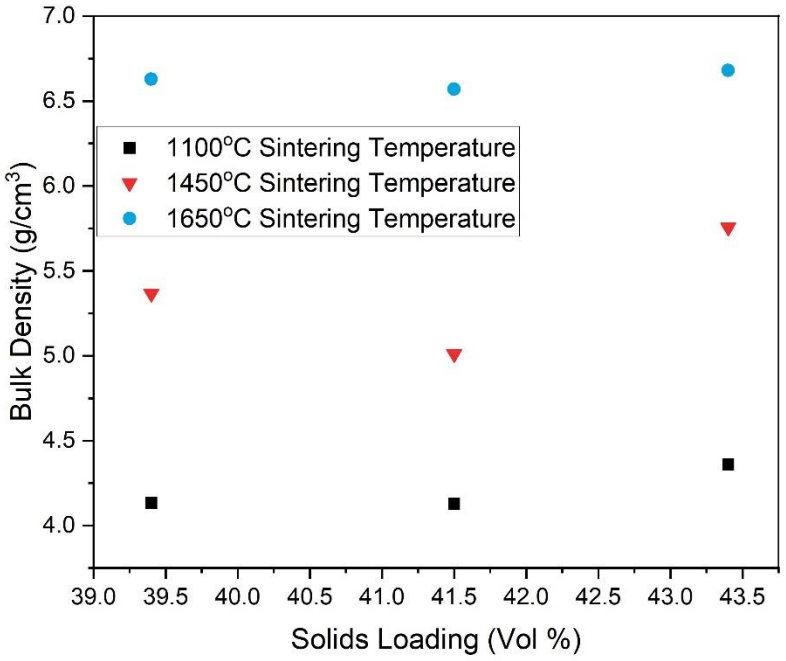

Figure 19. Effect of solid loading on bulk density of CeO_2, 2 µm particle size.

2. Microstructure Characterization

In addition to correlating density of the produced samples of the parametric study, the microstructural characterization was completed. Figure 20 – 30 show all SEM images collected with an accelerating voltage of 15 kV with a spot size of between 4.1 and 5.0. Magnification of the images was dependent on image quality for each sample, individually. Charging occurred on the surface of the low-density samples and therefore images were not taken at high magnifications for those samples.

Images were taken of the top surface of the printed as well as pressed samples. The surface was "as-printed" with no etching, polishing or other sample preparation. Grain boundaries were clearly seen and this view was used for grain size measurements. The internal microstructure and the interface between the internal cross section and the outer edge of the sample were also imaged. The internal microstructure showed open and closed pores along with grain boundaries. The internal cross section was not polished or etched and therefore most internal grain boundaries could not be seen. Grainsize measurements were taken on the top surface of the samples. The edge interface images gave an insight to

the layering effects of the print process and how the edge defects controlled the internal microstructure of the sample.

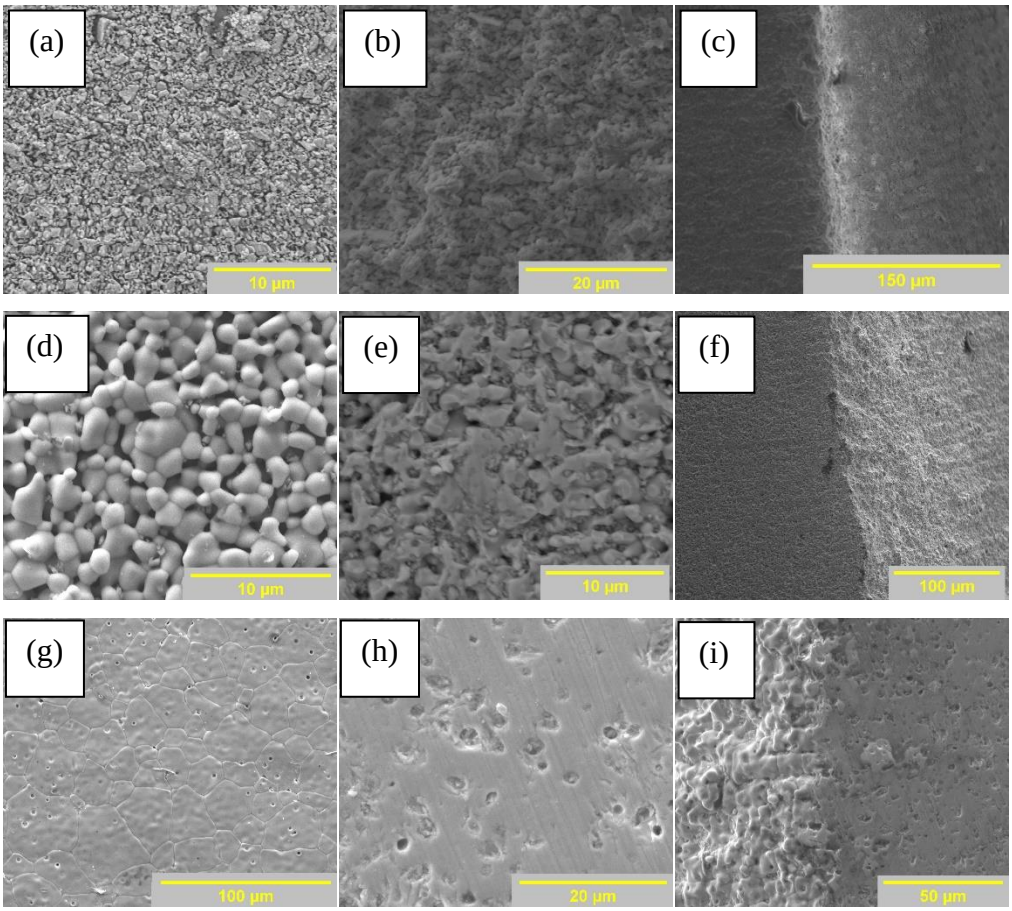

Figure 20. Samples printed with 39 vol%, 1 µm particle size powder, (a) top view, (b) cross section view, (c) edge interface view of sample sintered at 1100˚C; (d) top view, (e) cross section view, (f) edge interface view of sample sintered at 1450˚C; (g) top view, (h) cross section view, (i) edge interface view of sample sintered at 1650˚C.

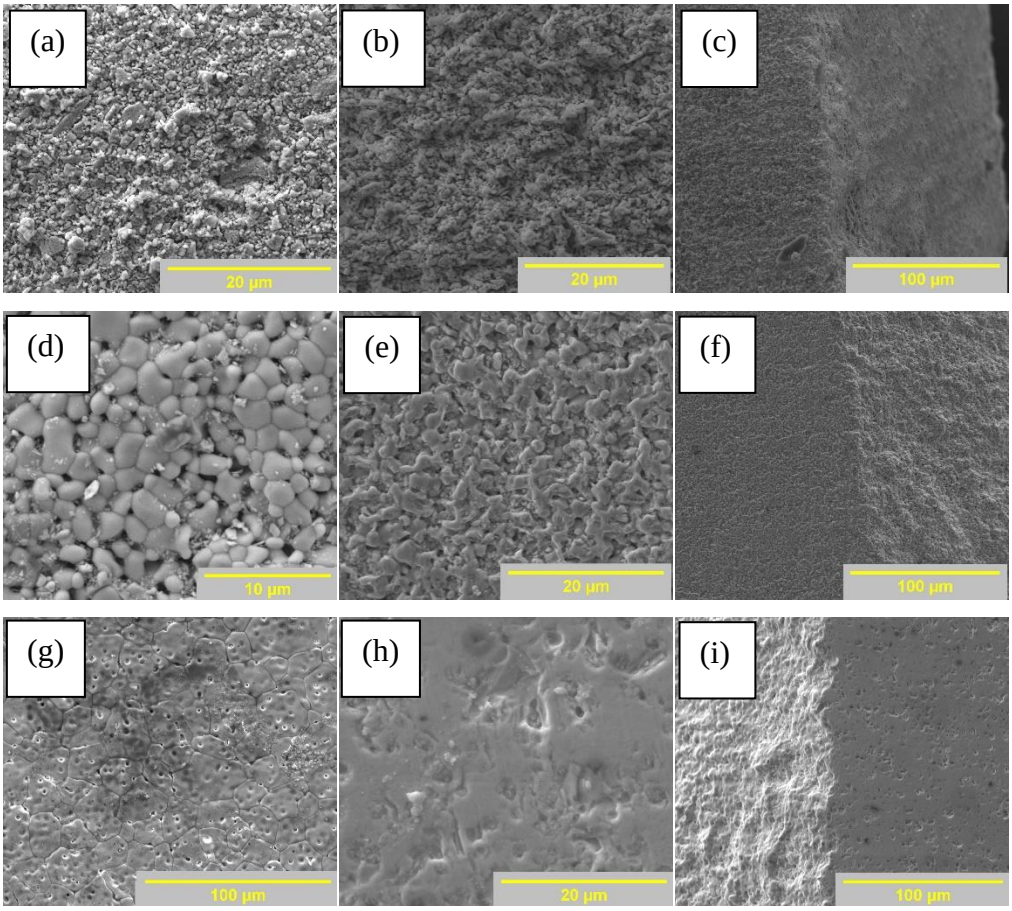

Figure 21. Samples printed with 41.5 vol%, 2 µm particle size powder, (a) top view, (b) cross section view, (c) edge interface view of sample sintered at 1100°C; (d) top view, (e) cross section view, (f) edge interface view of sample sintered at 1450°C; (g) top view, (h) cross section view, (i) edge interface view of sample sintered at 1650°C.

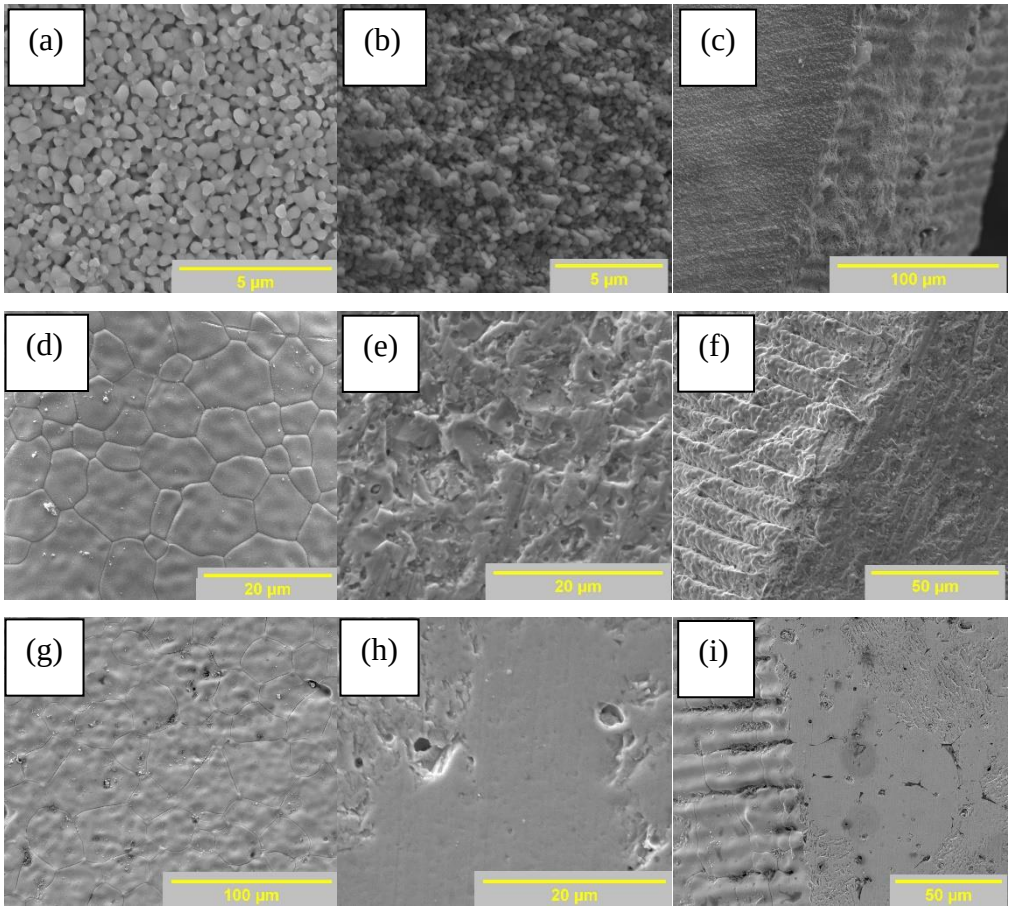

Figure 22. Samples printed with 39 vol%, 0.5 µm particle size powder, (a) top view, (b) cross section view, (c) edge interface view of sample sintered at 1100°C; (d) top view, (e) cross section view, (f) edge interface view of sample sintered at 1450°C; (g) top view, (h) cross section view, (i) edge interface view of sample sintered at 1650°C.

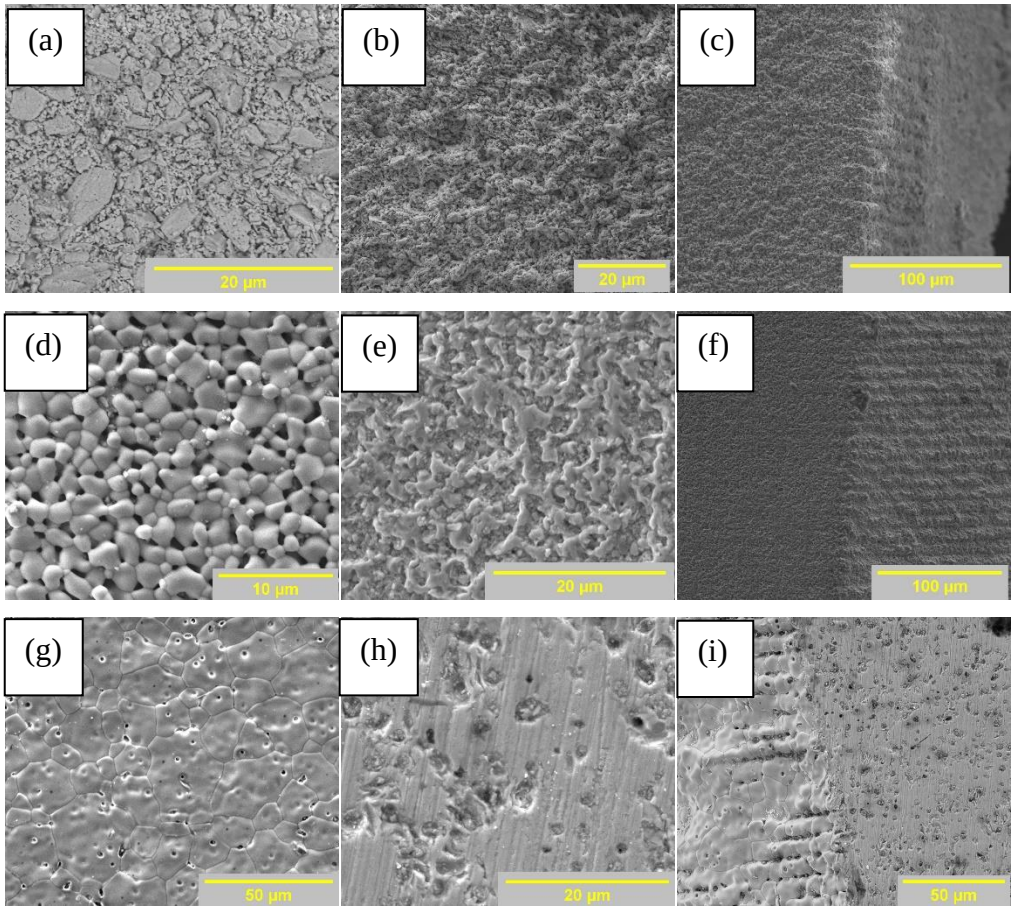

Figure 23. Samples printed with 37 vol%, 1 µm particle size powder, (a) top view, (b) cross section view, (c) edge interface view of sample sintered at 1100°C; (d) top view, (e) cross section view, (f) edge interface view of sample sintered at 1450°C; (g) top view, (h) cross section view, (i) edge interface view of sample sintered at 1650°C.

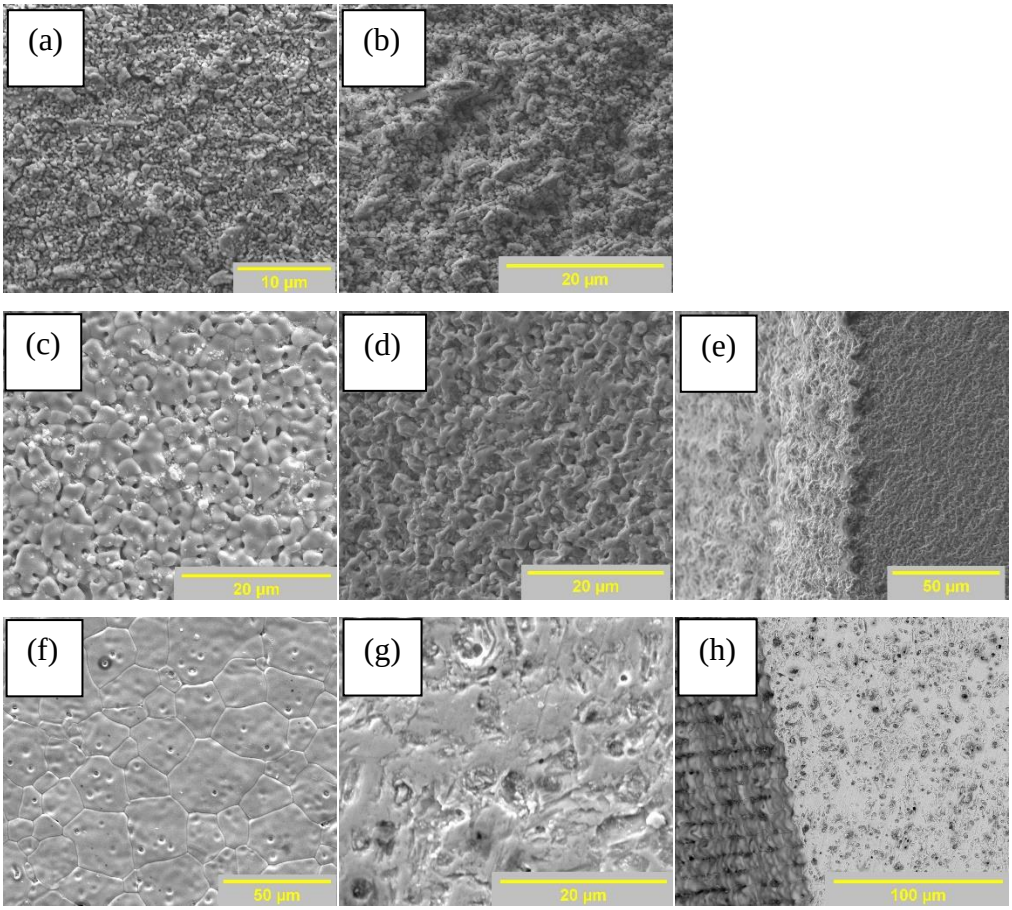

Figure 24. Samples printed with 39.4 vol%, 2 µm particle size powder, (a) top view, (b) cross section view of sample sintered at 1100˚C; (c) top view, (d) cross section view, (e) edge interface view of sample sintered at 1450˚C; (f) top view, (g) cross section view, (h) edge interface view of sample sintered at 1650˚C.

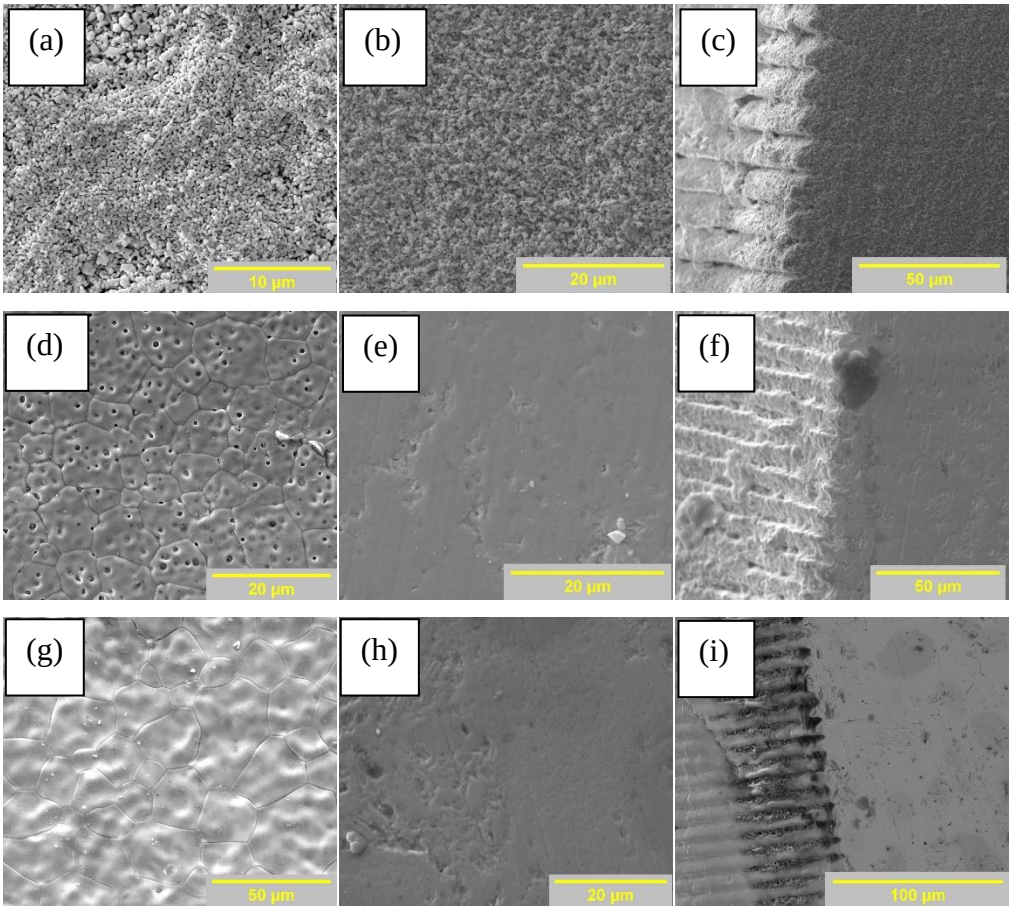

Figure 25. Samples printed with 37 vol%, 0.5 µm particle size powder, (a) top view, (b) cross section view, (c) edge interface view of sample sintered at 1100°C; (d) top view, (e) cross section view, (f) edge interface view of sample sintered at 1450°C; (g) top view, (h) cross section view, (i) edge interface view of sample sintered at 1650°C.

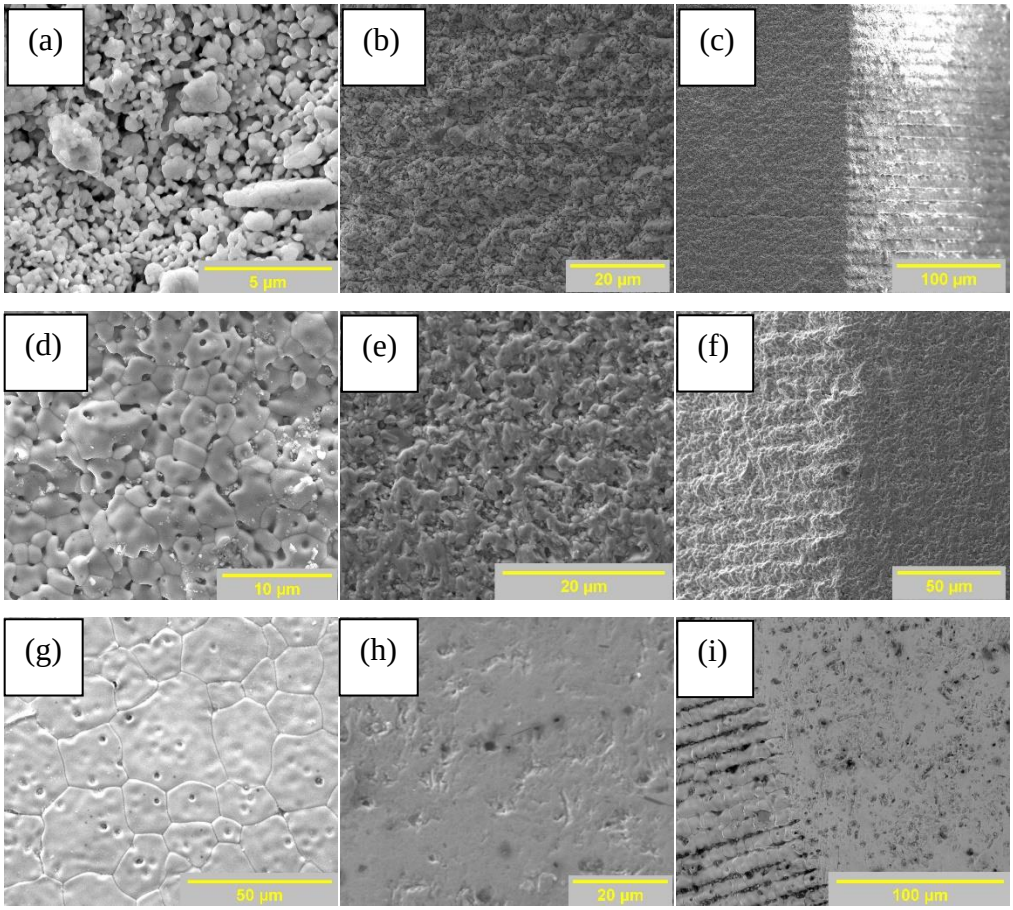

Figure 26. Samples printed with 41 vol%, 1 µm particle size powder, (a) top view, (b) cross section view, (c) edge interface view of sample sintered at 1100°C; (d) top view, (e) cross section view, (f) edge interface view of sample sintered at 1450°C; (g) top view, (h) cross section view, (i) edge interface view of sample sintered at 1650°C.

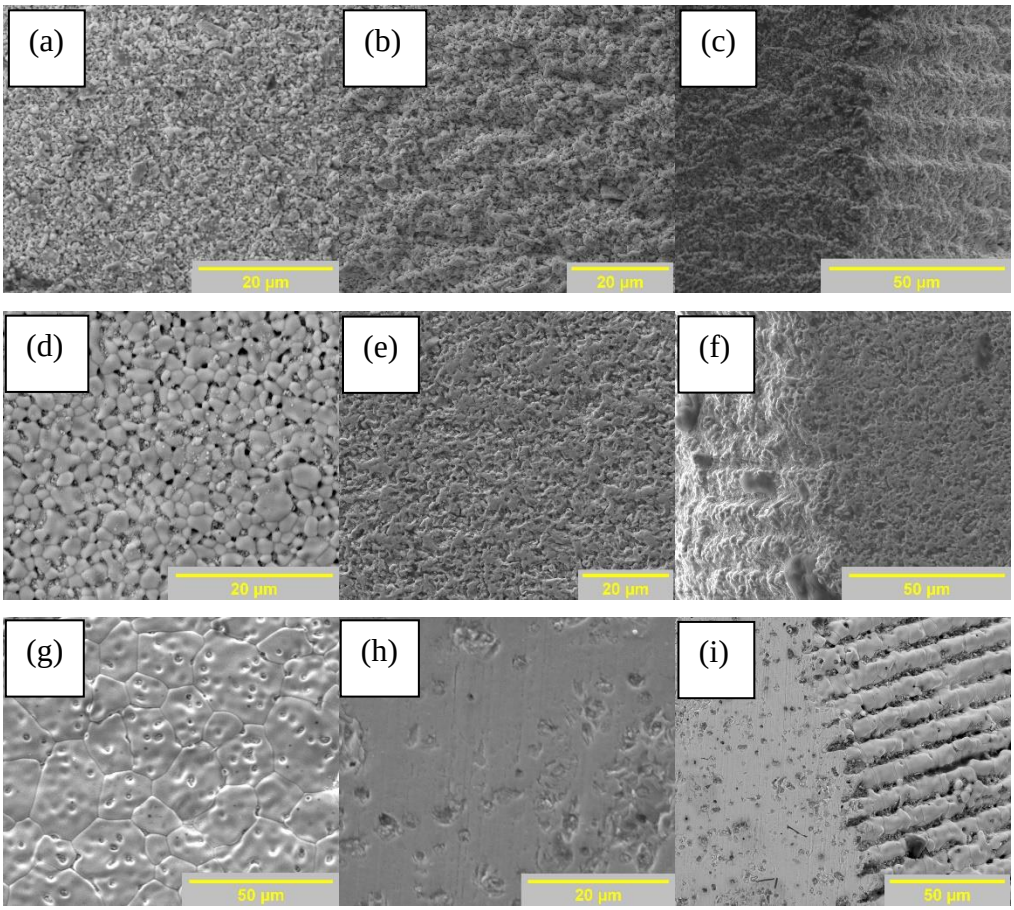

Figure 27. Samples printed with 43.4 vol%, 2 µm particle size powder, (a) top view, (b) cross section view, (c) edge interface view of sample sintered at 1100°C; (d) top view, (e) cross section view, (f) edge interface view of sample sintered at 1450°C; (g) top view, (h) cross section view, (i) edge interface view of sample sintered at 1650°C.

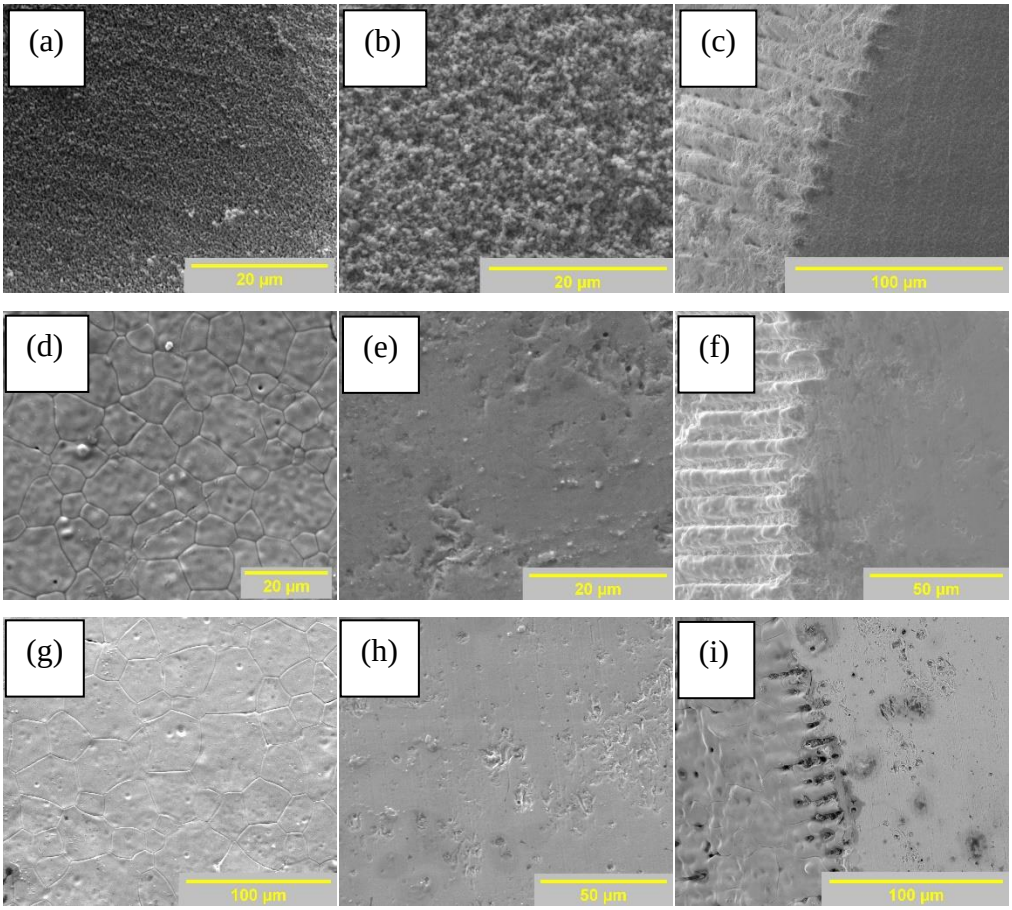

Figure 28. Samples printed with 41 vol%, 0.5 µm particle size powder, (a) top view, (b) cross section view, (c) edge interface view of sample sintered at 1100°C; (d) top view, (e) cross section view, (f) edge interface view of sample sintered at 1450°C; (g) top view, (h) cross section view, (i) edge interface view of sample sintered at 1650°C.

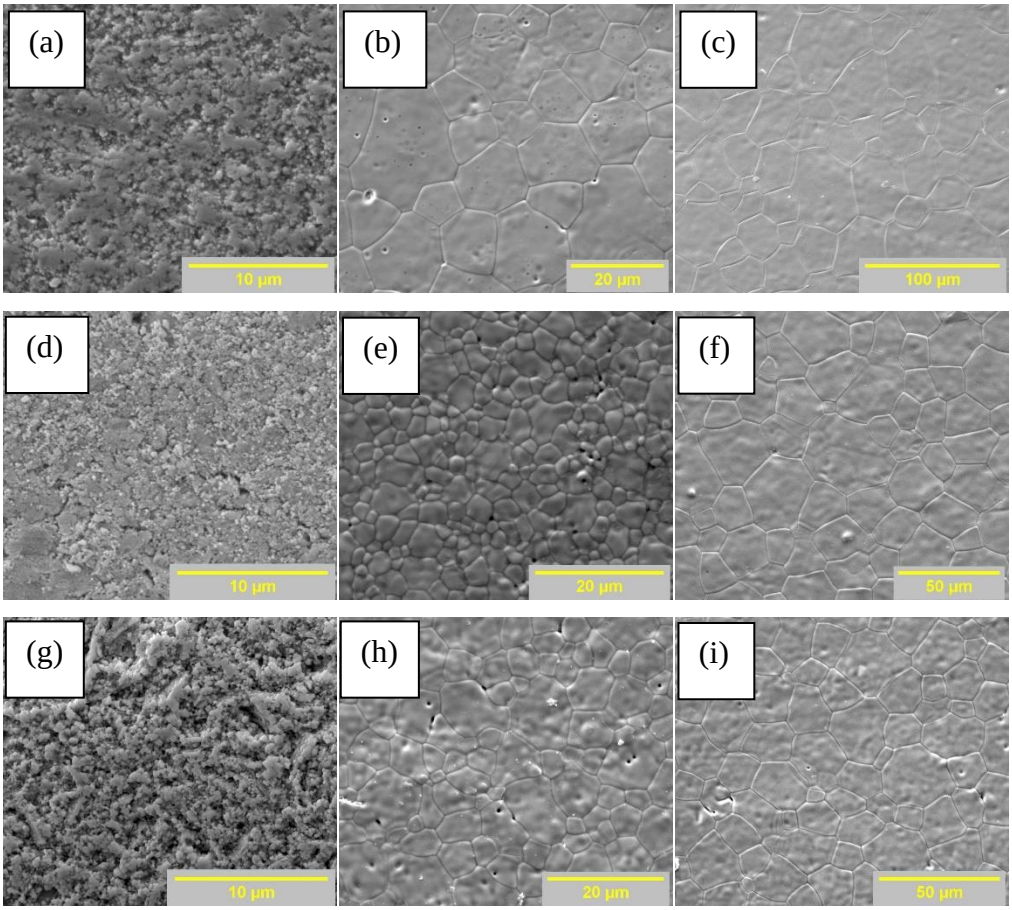

Figure 29. Sample pressed with 0.5 µm particle size powder and sintered at (a) 1100˚C, (b) 1450˚C, and (c) 1650˚C; sample pressed with 1 µm particle size powder and sintered at (d) 1100˚C, (e) 1450˚C, and (f) 1650˚C; sample pressed with 2 µm particle size powder and sintered at (g) 1100˚C, (h) 1450˚C, and (i) 1650˚C.

a. Effect of Solid Loading on Microstructure

No significant changes in microstructure were found when altering solid loading. Particle size and sintering temperature however, showed a range of porosity and grain size.

b. Effect of Sintering Temperature on Microstructure

Figure 30. shows the effect of sintering temperature on the microstructure. Figure 30 (a) shows the top view of a sample that was sintered at 1100˚C, Figure 30 (b) a sample sintered at 1450˚C, and (c) a sample sintered at 1650˚C. As expected, the samples sintered at 1100˚C have low density and open pores running through the sample. Small grains are visible showing some coalescing of the particles at the low sintering temperature. The sample sintered at 1450˚C, shown in Figure 30 (b), shows a higher density material with

grain boundaries clearly seen. Open pores can still be seen throughout the sample. The sample sintered at 1650˚C shows a reduction in porosity and pore size. The effect of sintering temperature on the microstructure was consistent between all three particle sizes and solid loadings.

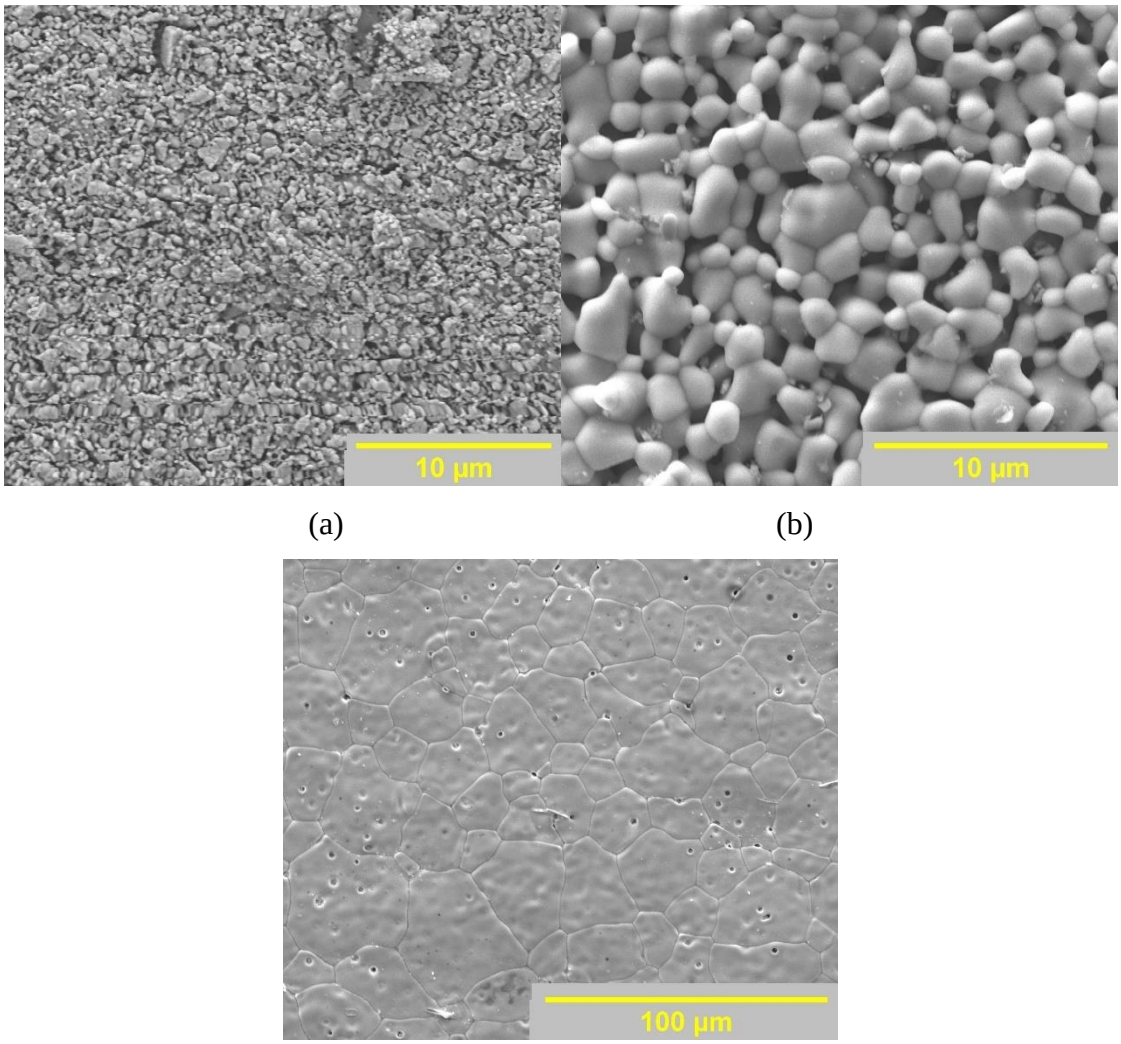

(a) (b)

(c)

Figure 30. Effect of sintering temperature on the microstructure of CeO_2, 1 µm particle size, high solid loading; Sample sintered at (a) 1100˚C, (b) 1450˚C (b), and (c) 1650˚C.

c. Effect of Particle Size on Microstructure

As shown in the density measurements, particle size had a significant effect on the printed samples. Figure 31 shows how particle size affects the grains and porosity of the

printed samples e. g., a sample printed with 1 µm (a), 2 µm (b), and 0.5 µm (c) particle size powders. These samples were sintered at 1450°C. Figure 31 (a) and (b) show similar structures with 1.611 µm and 1.655 µm average grain size with 29.47 vol% and 29.04 vol% apparent open porosity, respectively. Figure 31 (c) had 0.9% apparent open porosity and a larger average grain size of 6.908 µm. Grain size and standard deviation measurements for each printed and pressed sample are shown in the appendix.

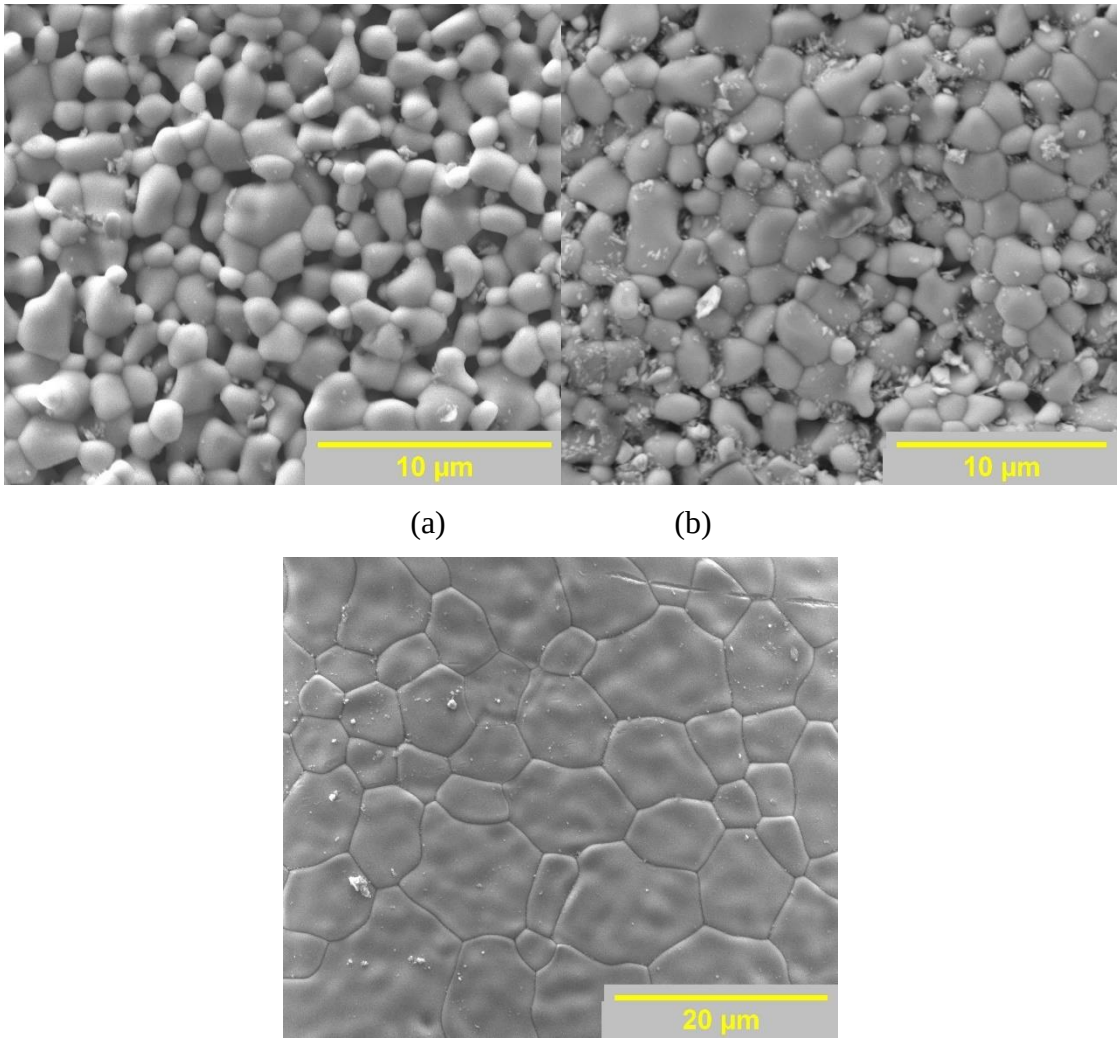

(a) (b)

(c)

Figure 31. Effect of particle size on the microstructure of CeO_2, sintered at 1450°C, medium solid loading; (a) Sample printed with 1 µm particle size powder, (b) Sample printed with 2 µm particle size powder, and (c) Sample printed with 0.5 µm particle size powder.

d. Effect of Parameters on Grain Size

Average grain size of the printed samples was strongly dependent on the particle size of the CeO_2 powder used in the slurry as well as the sintering temperature. The 0.5 µm powder consistently had larger grain sizes than the comparable 1 and 2 µm powder samples (Figure 32). Solid loading showed an effect on the 0.5 µm powders but there was no evidence of correlation in the 1 and 2 µm powder samples (Figure 33). As expected, sintering temperature showed a strong positive correlation with average grain size. The grain size followed an exponential growth curve between each sintering temperature (Figure 34).

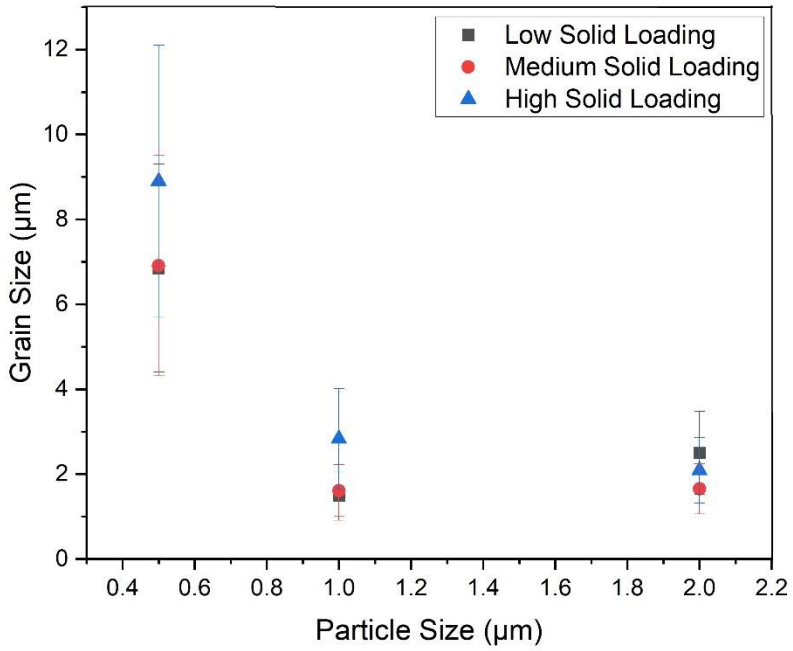

Figure 32. Effect of particle size on grain size of CeO_2, sintered at 1100˚C.

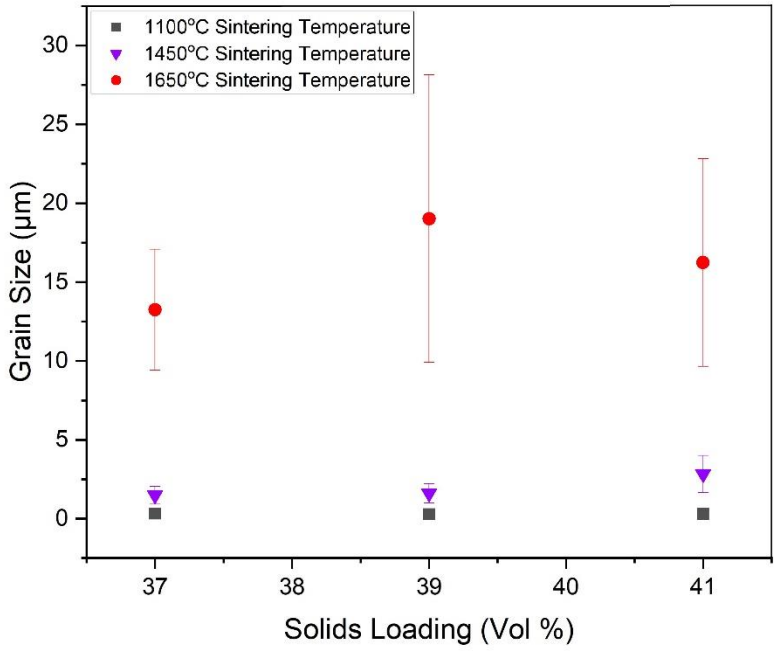

Figure 33. Effect of solid loading on grain size of CeO_2, 1 µm particle size.

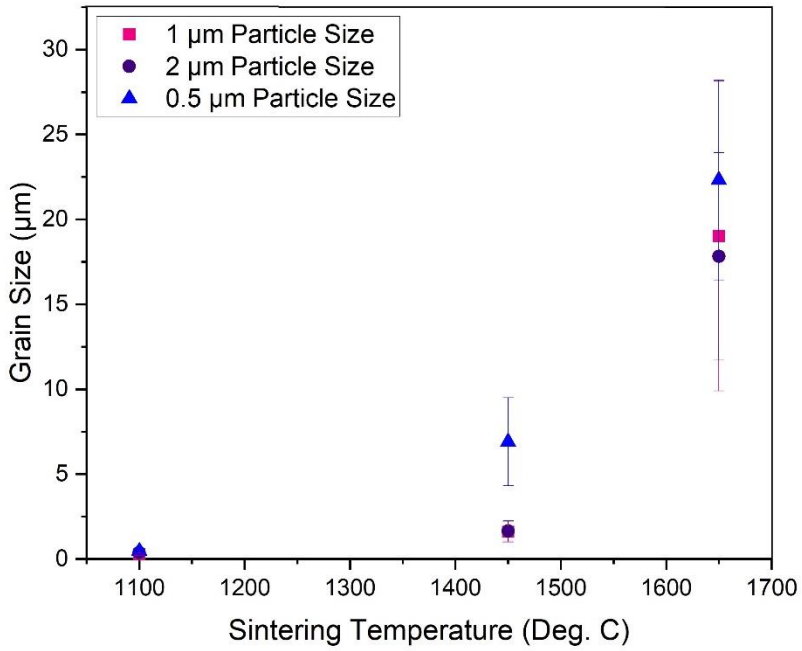

Figure 34. Effect of sintering temperature on grain size of CeO_2, medium solid loading.

3. XPS Analysis

XPS analysis was carried out to quantify the fractional concentration of oxidation states of cerium in the printed samples. Reference samples from literature were used for peak indexing[18]. Figure 35 shows a stacked plot of XPS spectra taken of all samples sintered at 1450°C. Surface roughness on the samples introduced some noise in the measured spectra, therefore a Savitzky-Golay smoothing[30] was completed for each. A representative spectrum was selected from the sample catalog and sample 9.b (0.5 µm powder, high solid loading, 1450°C sintering temperature) is shown in Figure 36. The spectrum was smoothed using Savitzky-Golay method and peaks corresponding to V_o, V, V', V'', V''', u_o, u, u', u'', and u''' were identified. The summation of the fitted peaks is shown in Figure 36.

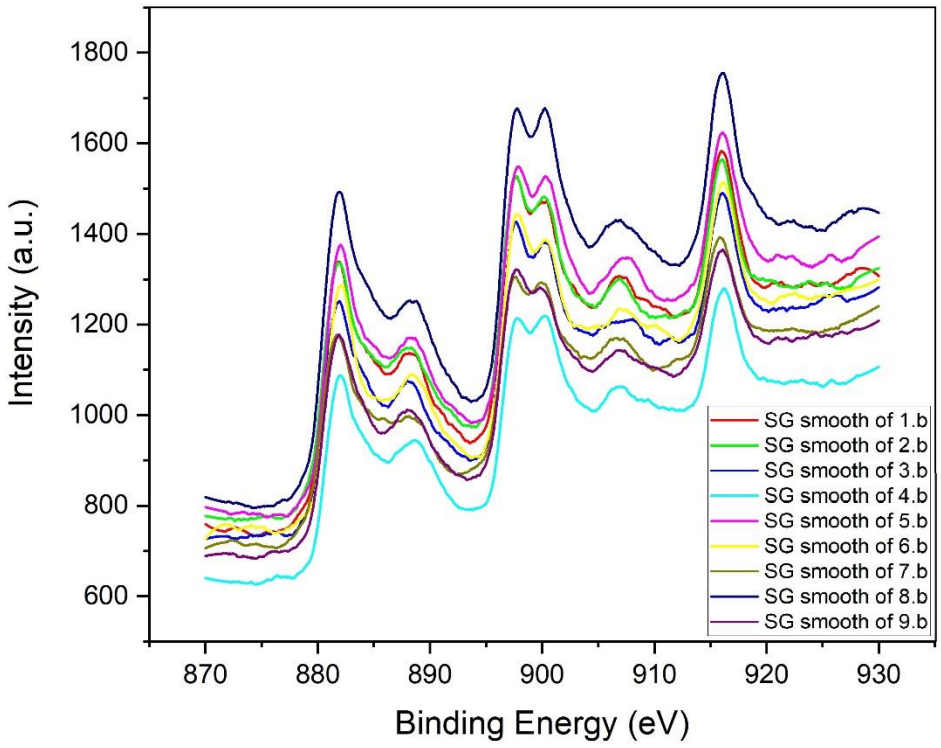

Figure 35. XPS spectra of all 9 measured samples.

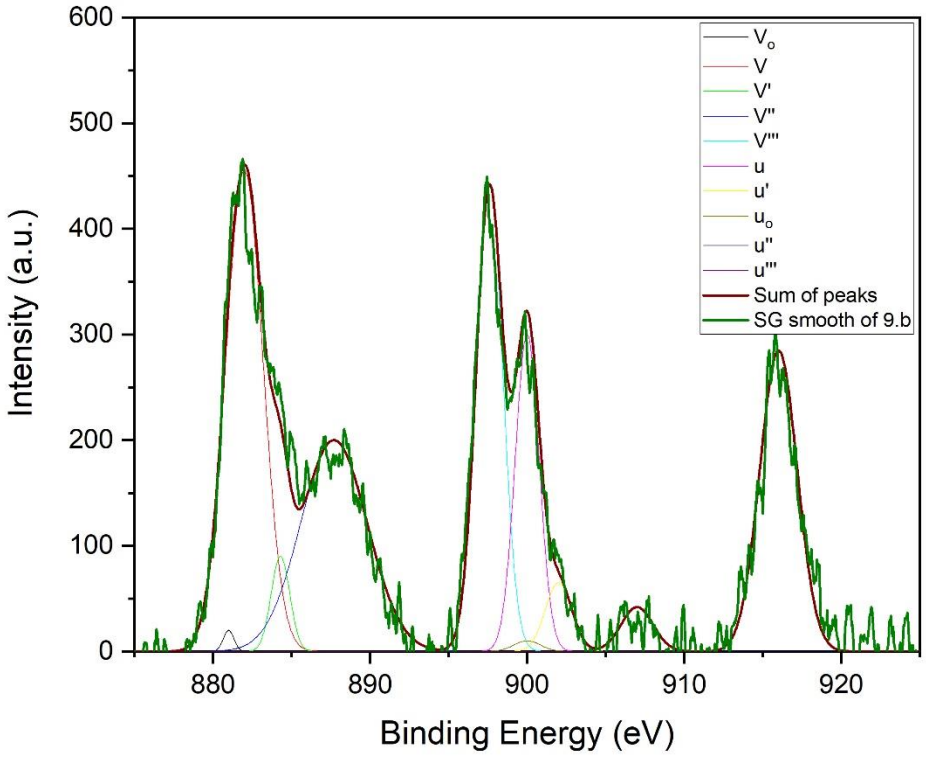

Figure 36. XPS spectra and fitted peaks for sample with 41 vol% solid loading and 0.5 µm particle size powder.

Following the spectrum smoothing and peak fitting, the area under each peak curve was used for quantitative analysis of Ce(III) concentration in the samples. Table 7 shows summation of each peak for the corresponding oxidation state of Ce along with the fractional concentration of Ce(III) in percentage calculated. From the measured data, no significant variation in Ce oxidation was found between the samples. The small amount of Ce(III) that was found (~ 5.5%) could be a result of charging of the samples from the x-ray source, the ultra-high vacuum environment when being measured in the XPS or the decomposition and off gassing of the binder during binder burnout[18, 31].

Table 7. Effect of Particle Size and Solid Loading on Fractional Concentration of Ce(III)

Sample	Particle Size	Solid Loading	Ce(III)	Ce(IV)	[Ce(III)] (%)
7.b	1	High (41 vol%)	428.27	6888.48	5.85
8.b	2	High (43.4 vol%)	565.57	8873.34	5.99
9.b	0.5	High (41 vol%)	487.69	7755.09	5.92
8.b	2	High (43.4 vol%)	565.57	8873.34	5.99
2.b	2	Medium (41.5 vol%)	516.86	7899.04	6.14
5.b	2	Low (39.4 vol%)	608.67	9285.28	6.15

a. Layering Effects caused by Printing Process

The layering effects from the printing process were also investigated. Images were taken showing the edge of the samples and how the layering effects the internal microstructure. Figure 37 shows the layering and how it extends into the internal microstructure of the samples. Pores are seen in the interlayer spacing however they do not follow the layering through the cross section of the sample. This result was consistent among all the samples. The edge effect interlayer spacing and post-sintered layer height were measured ~ 1.5 µm and ~ 9.0 µm, respectively.

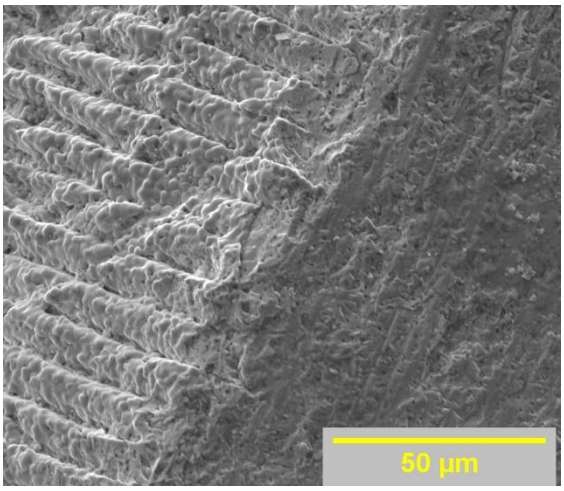

Figure 37. Layering effect on internal microstructure, 0.5 µm particle size, medium solid loading.

4. Printing Anomalies

Several artifacts from the printing process were observed in the printed samples. These included delamination between layers, a pitting effect on one surface of the sample, and a small convexity on the top surface of the parts.

Delamination was found in one sample with SEM imaging, as shown in Figure 38. Poor interlayer adhesion can cause cracking to occur in the interlayer spacing, also known as delamination. Shrinkage during sintering coupled with the off-gassing of the binder through open pores between layers are the main causes of delamination in ceramic AM parts[32, 33]. Maximum interlayer spacing in the delaminated section measured at ~1.3 µm and propagated ~165 µm into the part. This was the only instance of delamination that was found in the printed ceria samples. Polishing of the cross-sectional faces of more samples could prove to show more instances.

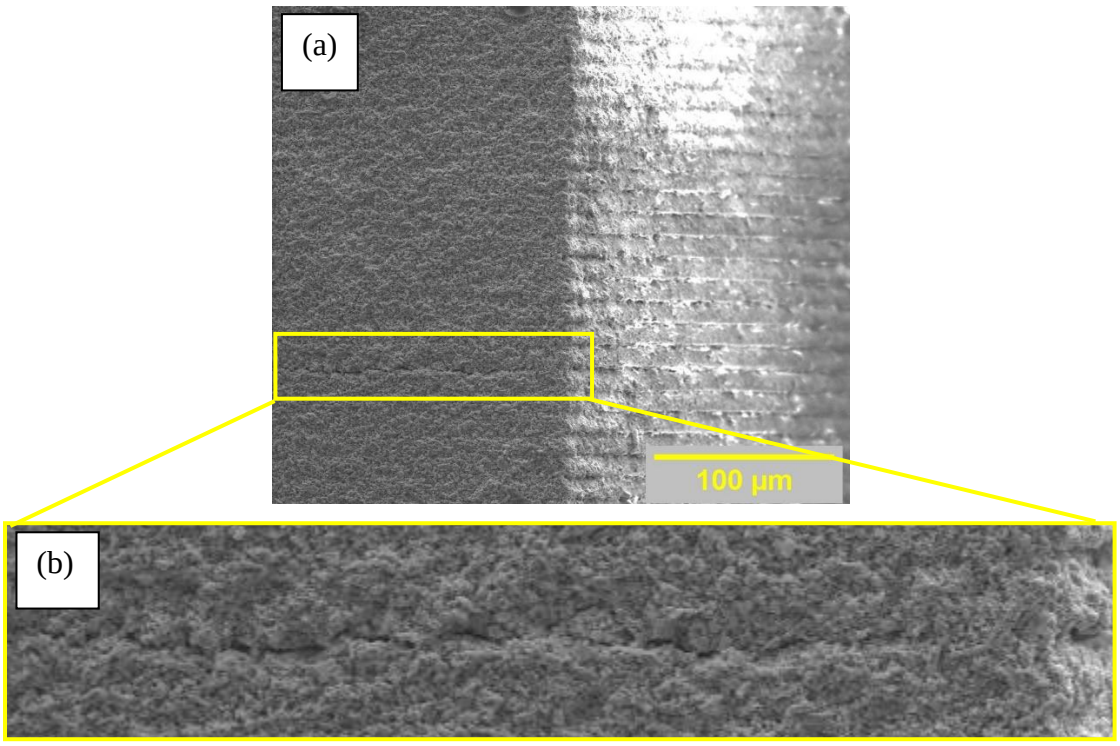

Figure 38. SEM micrograph of printed ceria sample (a) cross section-edge interface, (b) delamination between printed layers.

A pitting phenomenon was also seen on the top surface of the printed parts (Figure 39). This is caused by the liberation of gases from the inside of the printed parts during the debinding stage. Similar pitting has been seen in other materials and the investigations

documented[34-36]. As the gases rose through the samples during the post processing phases, gas filled closed pores propagated to the top surface from where the gases were released into the surrounding environment. A crater was left in its place, resulting in the pitting effect.

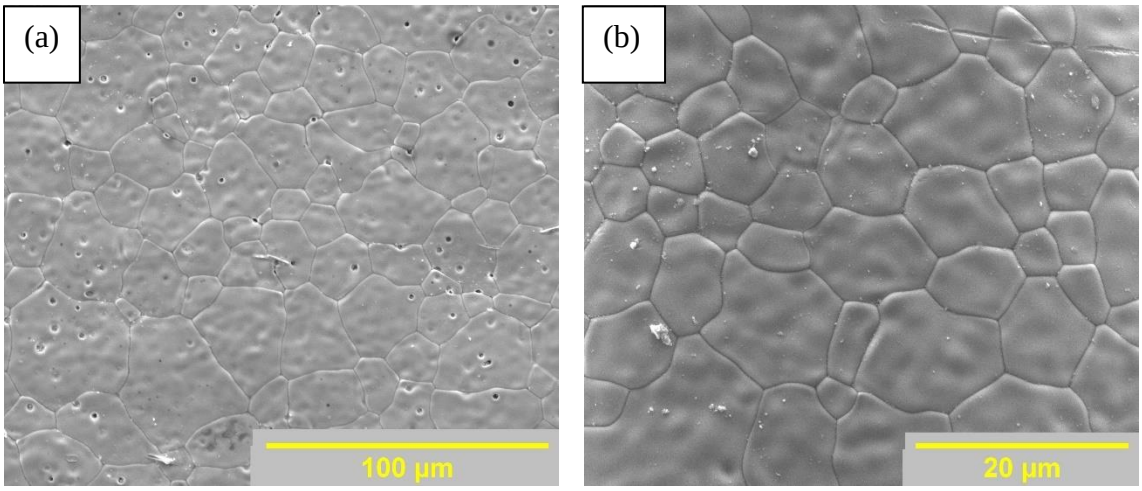

Figure 39. SEM micrographs of (a) top surface of printed ceria sample with pitting, (b) bottom surface of printed ceria sample without pitting.

In addition, the top surface of the printed samples also show a convexity protruding from the part (Figure 40). The cavitation from separating the printed part from the vat surface pulled a thin layer of uncured slurry onto the surface of the part. As the part was pressed back onto the vat surface to begin the next layer, the high viscosity slurry slightly indented the vat surface rather than push out from between the vat and the part surface. The continuation of this effect through the layering, slowly grew the convexity. A reduction in printing speed or viscosity of the slurry would help reduce this effect.

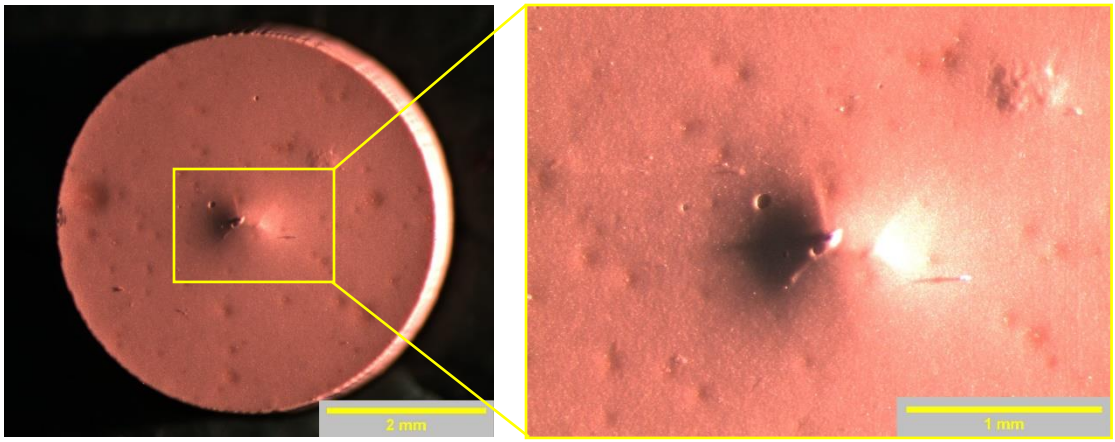

Figure 40. Image of convexity on sample surface.

V. SUMMARY AND CONCLUSIONS

The present study establishes the AM process parameters for ceria ceramics via LCM 3D printing based on the density and microstructure, values for particle size, sintering temperature, and solid loading. A parametric set of conditions that successfully produces dense printed parts is shown in Table A1 in the appendix. For production of high-density ceria ceramics with complex structures and geometries, 0.5 μm particle size CeO_2 powder with a slurry solid loading of 41.5 vol% is recommended. The optimal sintering temperature is found to be ~ 1450°C for the slurry formulation used, however, further investigations in sintering temperature and sintering time may lead to reduced grain growth while producing a low porosity solid. All ceria printing should be completed at an ambient temperature of ~ 30°C to reduce viscosity of the slurry during printing.

Powder particle size and sintering temperature have a prominent effect on the bulk density of the printed samples. The smallest particle size powder, 0.5 μm, produces the highest sintered density at each sintering temperature and solid loading. The bulk density for comparable pressed pellets remains relatively constant between each particle size. The effect of sintering temperature on the samples is also consistent across each particle size. Raising the maximum sintering temperature raises the final bulk density, but also exhibits accelerated grain growth at higher sintering temperatures, i.e., > 1450°C. Solid loading has a very minimal effect on the bulk density of the final sample. The density increases from the medium solid loading to the high but show no significant change between the low to the medium solid loadings.

Altering solid loading does not produce any significant change in the microstructure of 3D-printed samples. However, varying particle size and sintering temperature produce a range of porosity and grain size. Open porosity range is 0.0 - 46.5 vol% and grain size range, 0.29 - 25.23 μm in the printed samples. The samples sintered at a low temperature of 1100°C had very low density and have a chalk-like consistency. Open pores were seen running through the cross section of the sample. Slight coalescing of the particles at the low sintering temperature was found that caused the material to hold its shape. The samples sintered at the medium temperature of 1450°C show a much higher density material with grain boundaries clearly visible. Open pores could still be seen throughout the sample with

very little closed porosity. The samples sintered at the highest temperature showed a reduction in open porosity and pore size, however closed pores were found in the internal microstructure. The 1 μm and 2 μm powders produced a higher amount of closed porosity when sintered at 1650°C.

Particle size had a significant effect on the printed samples microstructure. The smaller particle size, 0.5 μm, densified at a lower temperature than the larger 1 μm and 2 μm powders. This was consistent through the pressed samples as well as the printed samples. The layering effects from the printing process were found to be an edge effect and the internal microstructure was not significantly affected.

XPS results showed no significant variation of Ce(III) concentration between the printed samples. Surface roughness on the measured samples caused noise in the recorded spectra. The results were smoothed, and the corresponding electron binding energy peaks were fit. The smoothing length needed to produce a usable curve (N = 50) through the law of error propagation could increase the error in the measured results. In addition, other sources of error are possible surface charging, effects from the UHV and catalytic activity during binder burnout can account for the small amount of Ce(III) measured in the samples.

VI. **FUTURE WORK**

Studies on other LCM produced ceramics have been reported in the literature[23, 24, 37, 38] and comparisons could be made with experience with the ceria ceramics. Mechanical testing of 3D-printed and sintered ceria ceramics can confirm anisotropy of physical properties caused by layering in the manufacturing process.

The sintering schedule for LCM printed ceria ceramics can be further investigated and optimized. Altering sintering temperature as well as dwell periods and heating rates could improve the quality of the final samples produced. Single-stage debinding and sintering schedules could also be investigated as a way of improving throughput of the parts produced by AM.

Support structure implementation and design relies heavily on the effects of processing of the material in question. Complex geometries and support structure design could be investigated as an extension of the present study. This will be critical for scaling up the process for implementation in production.

VII. **REFERENCES**

1. Stojmenović, M.; Bošković, S.; Bučevac, D.; Prekajski, M.; Babić, B.; Matović, B.; Mentus, S., Electrical characterization of multidoped ceria ceramics. *Ceramics International* **2013,** *39* (2), 1249-1255.
2. Zhang, Z.; Yu, L.; Liu, W.; Song, Z., Surface modification of ceria nanoparticles and their chemical mechanical polishing behavior on glass substrate. *Applied Surface Science* **2010,** *256* (12), 3856-3861.
3. Jacobson, A. J., Materials for solid oxide fuel cells. *Chemistry of Materials* **2010,** *22* (3), 660-674.
4. Pagliari, F.; Mandoli, C.; Forte, G.; Magnani, E.; Pagliari, S.; Nardone, G.; Licoccia, S.; Minieri, M.; Di Nardo, P.; Traversa, E., Cerium oxide nanoparticles protect cardiac progenitor cells from oxidative stress. *ACS nano* **2012,** *6* (5), 3767-3775.
5. Suri, S., Synthesis, Structural and Magnetic Properties of Copper Doped Cerium Oxide Nanoparticles. **2010**.
6. Gates-Rector, S.; Blanton, T., The powder Diffraction File: A Quality Materials Characterization Database. . 2019.
7. Dutta, P.; Pal, S.; Seehra, M.; Shi, Y.; Eyring, E.; Ernst, R., Concentration of Ce^{3+} and oxygen vacancies in cerium oxide nanoparticles. *Chemistry of Materials* **2006,** *18* (21), 5144-5146.
8. Yabe, S.; Sato, T., Cerium oxide for sunscreen cosmetics. *Journal of Solid State Chemistry* **2003,** *171* (1-2), 7-11.
9. Gorte, R. J.; Kim, H.; Vohs, J. M., Novel SOFC anodes for the direct electrochemical oxidation of hydrocarbon. *Journal of Power Sources* **2002,** *106* (1-2), 10-15.
10. Shao, Z.; Haile, S. M., A high-performance cathode for the next generation of solid-oxide fuel cells. In *Materials for Sustainable Energy: A Collection of Peer-Reviewed Research and Review Articles from Nature Publishing Group*, World Scientific: 2011; pp 255-258.
11. Trovarelli, A., Catalytic properties of ceria and CeO_2-containing materials. *Catalysis Reviews* **1996,** *38* (4), 439-520.
12. Nicollet, C.; Waxin, J.; Dupeyron, T.; Flura, A.; Heintz, J.-M.; Ouweltjes, J. P.; Piccardo, P.; Rougier, A.; Grenier, J.-C.; Bassat, J.-M., Gadolinium doped ceria interlayers for Solid Oxide Fuel Cells cathodes: Enhanced reactivity with sintering aids (Li, Cu, Zn), and improved densification by infiltration. *Journal of Power Sources* **2017,** *372*, 157-165.
13. Steele, B. C., Appraisal of $Ce_{1-y}Gd_yO_{2-y/2}$ electrolytes for IT-SOFC operation at 500° C. *Solid state ionics* **2000,** *129* (1-4), 95-110.
14. Inaba, H.; Tagawa, H., Ceria-based solid electrolytes. *Solid state ionics* **1996,** *83* (1-2), 1-16.
15. Sims, C. M.; Maier, R. A.; Johnston-Peck, A. C.; Gorham, J. M.; Hackley, V. A.; Nelson, B. C., Approaches for the quantitative analysis of oxidation state in cerium oxide nanomaterials. *Nanotechnology* **2018,** *30* (8), 085703.
16. Ali, S. M.; Rosli, R. E.; Muchtar, A.; Sulong, A. B.; Somalu, M. R.; Majlan, E. H., Effect of sintering temperature on surface morphology and electrical properties of samarium-doped ceria carbonate for solid oxide fuel cells. *Ceramics International* **2015,** *41* (1), 1323-1332.

17. Kazlauskas, S.; Kežionis, A.; Šalkus, T.; Orliukas, A. F., Effect of sintering temperature on electrical properties of gadolinium-doped ceria ceramics. *Journal of Materials Science* **2015,** *50* (8), 3246-3251.
18. Zhang, F.; Wang, P.; Koberstein, J.; Khalid, S.; Chan, S.-W., Cerium oxidation state in ceria nanoparticles studied with X-ray photoelectron spectroscopy and absorption near edge spectroscopy. *Surface Science* **2004,** *563* (1-3), 74-82.
19. Schwentenwein, M.; Schneider, P.; Homa, J. In *Lithography-based ceramic manufacturing: a novel technique for additive manufacturing of high-performance ceramics*, Advances in Science and Technology, Trans Tech Publ: 2014; pp 60-64.
20. Eckel, Z. C.; Zhou, C.; Martin, J. H.; Jacobsen, A. J.; Carter, W. B.; Schaedler, T. A., Additive manufacturing of polymer-derived ceramics. *Science* **2016,** *351* (6268), 58-62.
21. David L. Bourell, C. E. R. Photonics Applied: 3D Laser Printing: Selecting and using materials for additive manufacturing processes. https://www.laserfocusworld.com/lasers-sources/article/16548177/photonics-applied-3d-laser-printing-selecting-and-using-materials-for-additive-manufacturing-processes.
22. Johannes, H.; Patzer, J.; Reiter, R.; Spitzbart, M., Method for the layered construction of a shaped body. Google Patents: 2020.
23. Schwentenwein, M.; Homa, J., Additive manufacturing of dense alumina ceramics. *International Journal of Applied Ceramic Technology* **2015,** *12* (1), 1-7.
24. Altun, A. A.; Prochaska, T.; Konegger, T.; Schwentenwein, M., Dense, strong, and precise silicon nitride-based ceramic parts by lithography-based ceramic manufacturing. *Applied Sciences* **2020,** *10* (3), 996.
25. Akopov, F.; Poluboyarinov, D., Some properties of sintered ceria ceramics. *Refractories* **1965,** *6* (3-4), 196-201.
26. Zaengle, T. H.; Ndayishimiye, A.; Tsuji, K.; Fan, Z.; Bang, S. H.; Perini, J.; Misture, S. T.; Randall, C. A., Single-step densification of nanocrystalline CeO_2 by the cold sintering process. *Journal of the American Ceramic Society* **2020,** *103* (5), 2979-2985.
27. Slusser, P. K. Transition metal doped cerium oxide for spintronics applications. Department of Materials Science and Engineering, University of Utah, 2009.
28. Agersted, K. In *Sintering doped Ceria in air*, Nordic Conference on Ceramic and Glass Technology, 2012.
29. Chen, J.-C.; Chen, W.-C.; Tien, Y.-C.; Shih, C.-J., Effect of calcination temperature on the crystallite growth of cerium oxide nano-powders prepared by the co-precipitation process. *Journal of alloys and compounds* **2010,** *496* (1-2), 364-369.
30. Cumpson, P., Guide to smoothing in AES and XPS. **1998**.
31. Masia, S.; Calvert, P. D.; Rhine, W. E.; Bowen, H. K., Effect of oxides on binder burnout during ceramics processing. *Journal of materials science* **1989,** *24* (6), 1907-1912.
32. Pepin, J. G.; Borland, W.; O'Callaghan, P.; Young, R. J., Electrode-Based Causes of Delaminations in Multilayer Ceramic Capacitors. *Journal of the American Ceramic Society* **1989,** *72* (12), 2287-2291.
33. Levikari, S.; Kärkkäinen, T. J.; Andersson, C.; Tammminen, J.; Silventoinen, P., Acoustic detection of cracks and delamination in multilayer ceramic capacitors. *IEEE Transactions on Industry Applications* **2018,** *55* (2), 1787-1794.

34. Jacobson, N.; Smialek, J., Corrosion pitting of SiC by molten salts. *Journal of the Electrochemical Society* **1986,** *133* (12), 2615.
35. Wang, N.; Wang, S.; Liu, G.; Zhang, Y.; Zhao, K.; Ren, B.; Wang, Y., In situ high-entropy solid solution and ceramic particles co-reinforced Ni-based composites with outstanding strength-ductility synergy and good pitting resistance. *Materials Science and Engineering: A* **2021**, 140842.
36. Torrens, R.; Sammes, N.; Tompsett, G., Characterisation of $(CeO_2)_{0.8}(GdO_{1.5})_{0.2}$ synthesised using various techniques. *Solid State Ionics* **1998,** *111* (1-2), 9-15.
37. An, D.; Li, H.; Xie, Z.; Zhu, T.; Luo, X.; Shen, Z.; Ma, J., Additive manufacturing and characterization of complex Al_2O_3 parts based on a novel stereolithography method. *International Journal of Applied Ceramic Technology* **2017,** *14* (5), 836-844.
38. Zanchetta, E.; Cattaldo, M.; Franchin, G.; Schwentenwein, M.; Homa, J.; Brusatin, G.; Colombo, P., Stereolithography of SiOC ceramic microcomponents. *Advanced Materials* **2016,** *28* (2), 370-376.

VIII. **APPENDIX**

Table A1. Print Settings for All Ceria Printed Samples

Parameter	
Layer Thickness (µm)	15
Support Structure Thickness (µm)	300
Contour Offset (µm)	0
Pixel Alignment	Yes
Lateral (XY) shrinking compensation	1.13
Build direction (Z) shrinking compensation	1.25
Z curing depth compensation	No
Z curing depth compensation layers	0
Dispensation correction	1.2
Dispensation correction support	1.5
Angle of rotation start [rotations]	10
Angle of rotation general [rotations]	5
Rotation speed [°/s]	120
Settling time start [s]	180
Settling time general [s]	8
Tilt up speed start [°/s]	7
Tilt up speed general [°/s]	10
Backlight exposure time [s]	3
Settling time backlight layer [s]	120
DLP energy start [mJ/cm^2]	400
DLP energy general [mJ/cm^2]	300
Tilt down speed start [°/s]	2
Tilt down speed general [°/s]	4

Table A2. Grain Size Measurements for All Ceria Samples

Sample Name	Solid loading (Vol %)	Particle Size (μm)	Sintering Temperature (Deg. C)	Grain Size (μm)	Grain Size St. Dev. (μm)
1a	39	1	1100	0.286	0.059
2a	41.5	2	1100	0.377	0.111
3a	39	0.5	1100	0.467	0.151
4a	37	1	1100	0.325	0.095
5a	39.4	2	1100	0.321	0.080
6a	37	0.5	1100	0.271	0.066
7a	41	1	1100	0.289	0.090
8a	43.4	2	1100	0.370	0.142
9a	41	0.5	1100	0.379	0.111
1um.a	Pressed	1	1100	0.270	0.082
2um.a	Pressed	2	1100	0.375	0.167
0.5um.a	Pressed	0.5	1100	0.248	0.075
1b	39	1	1450	1.611	0.611
2b	41.5	2	1450	1.655	0.595
3b	39	0.5	1450	6.908	2.597
4b	37	1	1450	1.484	0.566
5b	39.4	2	1450	2.495	0.979
6b	37	0.5	1450	6.852	2.450
7b	41	1	1450	2.835	1.177
8b	43.4	2	1450	2.095	0.773
9b	41	0.5	1450	8.896	3.207
1um.b	Pressed	1	1450	3.570	1.624
2um.b	Pressed	2	1450	5.624	2.417
0.5um.b	Pressed	0.5	1450	12.290	4.190
1c	39	1	1650	19.021	9.121
2c	41.5	2	1650	17.816	6.110
3c	39	0.5	1650	22.318	5.885
4c	37	1	1650	13.244	3.837
5c	39.4	2	1650	19.910	6.455
6c	37	0.5	1650	20.515	7.193
7c	41	1	1650	16.241	6.589
8c	43.4	2	1650	15.328	6.541
9c	41	0.5	1650	25.230	9.405
1um.c	Pressed	1	1650	17.794	5.600
2um.c	Pressed	2	1650	21.685	9.596
0.5um.c	Pressed	0.5	1650	29.798	8.665

Table A3. Density Measurements for Ceria Samples

Sample	Solids Loading (vol%)	Particle Size (μm)	Sintering Temperature (ºC)	Saturated Weight (g)	Suspended Weight (g)	Exterior Volume (cm^3)	Dry Weight (g)	Apparent Porisity (vol%)	Bulk Density (g/cm^3)	Open Pore Volume (cm^3)
1a	39	1	1100	0.241	0.186	0.055	0.215	46.404	3.932	0.025
2a	41.5	2	1100	0.251	0.196	0.055	0.227	43.267	4.117	0.024
3a	39	0.5	1100	0.235	0.186	0.048	0.216	38.540	4.452	0.019
4a	37	1	1100	0.235	0.182	0.053	0.211	44.501	3.984	0.024
5a	39.4	2	1100	0.241	0.189	0.053	0.219	42.804	4.124	0.023
6a	37	0.5	1100	0.228	0.180	0.049	0.209	40.390	4.255	0.020
7a	41	1	1100	0.248	0.194	0.054	0.225	41.873	4.195	0.022
8a	43.4	2	1100	0.259	0.204	0.054	0.237	39.240	4.349	0.021
9a	41	0.5	1100	0.250	0.198	0.052	0.231	37.116	4.456	0.019
1um.a	Pressed	1	1100	2.521	2.092	0.430	2.433	20.428	5.649	0.088
2um.a	Pressed	2	1100	2.537	2.113	0.424	2.457	18.760	5.776	0.080
0.5um.a	Pressed	0.5	1100	2.519	2.103	0.417	2.442	18.561	5.848	0.077
1b	39	1	1450	0.230	0.187	0.043	0.217	29.393	5.031	0.013
2b	41.5	2	1450	0.243	0.197	0.046	0.230	28.967	4.998	0.013
3b	39	0.5	1450	0.216	0.183	0.033	0.216	0.918	6.594	0.000
4b	37	1	1450	0.219	0.178	0.040	0.207	28.394	5.111	0.011
5b	39.4	2	1450	0.230	0.189	0.041	0.220	25.302	5.352	0.010
6b	37	0.5	1450	0.209	0.178	0.031	0.209	0.324	6.756	0.000
7b	41	1	1450	0.235	0.195	0.040	0.227	20.000	5.673	0.008
8b	43.4	2	1450	0.242	0.202	0.041	0.234	19.607	5.742	0.008

9b	41	0.5	1450	0.231	0.197	0.034	0.231	0.298	6.866	0.000
1um.b	Pressed	1	1450	2.461	2.103	0.358	2.458	0.780	6.848	0.003
2um.b	Pressed	2	1450	2.354	2.009	0.345	2.350	1.157	6.797	0.004
0.5um.b	Pressed	0.5	1450	2.410	2.061	0.349	2.405	1.488	6.881	0.005
1c	39	1	1650	0.213	0.181	0.032	0.212	0.929	6.580	0.000
2c	41.5	2	1650	0.228	0.194	0.035	0.228	0.575	6.554	0.000
3c	39	0.5	1650	0.215	0.184	0.030	0.214	0.329	7.058	0.000
4c	37	1	1650	0.209	0.178	0.031	0.209	0.000	6.707	0.000
5c	39.4	2	1650	0.223	0.190	0.034	0.223	0.000	6.613	0.000
6c	37	0.5	1650	0.207	0.178	0.029	0.207	0.343	7.096	0.000
7c	41	1	1650	0.229	0.195	0.035	0.229	0.288	6.605	0.000
8c	43.4	2	1650	0.235	0.200	0.035	0.235	0.284	6.664	0.000
9c	41	0.5	1650	0.230	0.197	0.033	0.230	0.000	7.016	0.000
1um.c	Pressed	1	1650	2.443	2.093	0.350	2.440	0.969	6.952	0.003
2um.c	Pressed	2	1650	2.410	2.065	0.345	2.407	0.955	6.966	0.003
0.5um.c	Pressed	0.5	1650	2.398	2.054	0.343	2.394	1.163	6.957	0.004